Controlling Cold Collisions of Polar Molecules with External Fields

by

Christopher Carl Ticknor

B.S., Bucknell Univeristy, 2001

M.S., University of Colorado, 2004

A thesis submitted to the

Faculty of the Graduate School of the

University of Colorado in partial fulfillment

of the requirements for the degree of

Doctor of Philosophy

Department of Physics

2005

This thesis entitled:
Controlling Cold Collisions of Polar Molecules with External Fields
written by Christopher Carl Ticknor
has been approved for the Department of Physics

John L. Bohn

Murray Holland

Date

The final copy of this thesis has been examined by the signatories, and we find that both the content and the form meet acceptable presentation standards of scholarly work in the above mentioned discipline.

Ticknor, Christopher Carl (Ph.D., Physics)

Controlling Cold Collisions of Polar Molecules with External Fields

Thesis directed by Prof. John L. Bohn

In this thesis we explore how external fields can be used to control collisions of ultracold polar molecules. First we review the Stark and Zeeman effects for polar molecules and two body multi-channel scattering theory. A general treatment of the Stark effect and dipolar interactions is also presented. We consider cold collisions of OH molecules in the $^2\Pi_{3/2}$ ground state under the influence of a magnetic field. We find that modest fields of several thousand Gauss can act to suppress inelastic collisions of weak-field-seeking states by two orders of magnitude. We attribute this suppression to two factors: (i) an indirect coupling of the entrance and the exit channel, in contrast to the effect of an applied electric field and (ii) the relative shift of the entrance and exit scattering thresholds. In view of these results, magnetic trapping of OH may prove experimentally feasible.

We also present first steps toward understanding the ultracold scattering properties of polar molecules in strong electric field-seeking states. We have found that the elastic cross section displays a quasi-regular set of potential resonances as a function of the electric field, which potentially offers intimate details about the intermolecular interaction. We illustrate these resonances using a "toy" model composed of pure dipoles and a more physically realistic system. To analyze these resonances, we use a simple WKB approximation to the eigenphase, which proves both reasonably accurate and meaningful.

Acknowledgements

First, I will acknowledge and thank all those that helped me get through graduate school by climbing and road biking with me. Then I would like to thank the ones I love for their support, my parents and Alison.

I would like to thank the members of the Bohn group for their various contributions: D. C. E. Bortolotti, A. Avdeenkov, A. Volpi, M. Lara, and E. Meyer.

I wish to acknowledge and thank the experimentalists I worked with, who truly made graduate school a learning experience: T. Loftus, C. A. Regal, M. Griener, S. Inouye, J. Goldwin, M. L. Olsen, and D. S. Jin.

Finally I would like to thank John L. Bohn for his patience, incredible willingness to teach, and enthusiasm for science.

Contents

Chapter

Tables

Table

Figures

Figure

Chapter 1

Introduction

Dipoles and their interactions constitute a dominant driving force behind the structure and physical properties of matter. Aspects of dipolar driven structure can be found in plasmas [1], biomolecular fluids [2, 3], magnetic materials [4, 5], and semiconductors [4, 6, 7]. Such systems display fantastically rich collective behavior originating from anisotropic dipolar interactions. For example, the dipolar interaction can induce phase transitions, in which the systems become more ordered such as when a ferromagnet is cooled below its Curie temperature, the dipoles begin to align and the macroscopic system gains macroscopic order [8]. Dipolar interactions can also have subtle, yet significant, effects, such as in high T_C superconductors where magnetic order plays a significant role in their properties [9, 10, 11, 12, 13].

Dipolar systems become even more intricate with the application of an external field that also interacts with the dipoles. This field can be used to control the dipoles and, consequently, the physical properties of the system. Examples can be found in such phenomena as colossal magneto-resistance [14], mesoscopic ferro-fluids [15, 16], or the phases of high T_C superconductors [17, 18, 19]. Since the dipole-dipole and field-dipole interactions determine the properties of many physical systems, it is desirable to understand them. Even simple models of dipoles have rich properties. For example, the Ising model is an array of fixed dipoles on a lattice that only interact with their nearest neighbors. This model displays phase transitions much like those found in ferromagnets

[8, 20].

However, physical systems are complicated and have many contributing interactions that lead to their physical properties; thus understanding their properties is difficult. The desire to gain insight into complex systems has led to the pursuit of relatively simple physical systems that can be studied and explored more throughly. The relatively new field of ultracold [1] atoms is a wonderful example of such systems [21]. A notable success of this field was the production of Bose-Einstein Condensation (BEC) in a gas composed of dilute alkali atoms in 1995 [22, 23, 24]. Since then, ultracold atomic systems have allured researchers to explore the fundamental properties of matter [25]. The techniques to control ultracold atoms that led to BEC have been used to create degenerate Fermi gases [26]. Furthermore, the ability to control atomic interactions has led to the study of the BEC-BCS crossover problem [27, 28, 29]. Such rapid advances have led to new insights into the properties of matter because these systems can the finely tuned, controlled and then explored.

With the tremendous success and advancements in ultracold atomic physics, scientists have begun to turn their attention towards polar molecules, with hopes of placing them in the ultracold environment [30]. We are excited about the possibilities that dipolar interaction will lead to strongly correlated systems, which can be finely controlled. Just as the study of ultracold alkali atoms yielded the ability to carefully study many-body systems, scientists speculate the investigation of ultracold polar molecules could lead to advances in the understanding of highly correlated, strongly interacting dipolar systems and even insight into dipolar phase transitions.

Exciting predictions have begun to emerge for ultracold dipolar systems; most predict novel collective properties [31]. These predictions include the creation of BECs with novel physical properties, exotic collective excitations [32, 33, 34], super-solid phase

[1] By convention, "cold" atomic gases have temperature equal to or less than 1 mK, and "ultracold" gases have temperatures roughly equal to or less than μK.

transitions in dipolar BECs [35], and novel types of pairing physics for fermions [36, 37, 38]. These possibilities are exciting because of insights they might offer in the fundamental properties of matter. Furthermore, they may have exciting applications, such as the use of ultracold polar molecules for robust quantum computing schemes [39].

At the heart of such predictions are the two-body dipolar collisions, which are not well understood. There is a growing need to understand these collision properties as the experiments begin to trap polar molecules. We need to understand the molecular collisional properties to build accurate predictions about their collective behavior and exploit them. It is the intention of this work to explore the theory of ultracold two-body collisions of polar molecules and to understand how external fields can be used to control the collisions.

In the next two sections we briefly review the current state of research into the production and understanding of ultracold molecules. We first present an overview of experimental methods [30], followed by a review of the state of theory for cold collisions of polar molecules.

1.1 Production of Cold Polar Molecules

One way to produce cold molecules is to start with cold atoms and then associate them. This can be achieved with a magnetic Feshbach resonance, i.e., using an applied magnetic field to alter the molecular structure of colliding pairs such that they can be dynamically converted into molecules. The use of these resonances to produce ultracold molecules has been experimentally demonstrated with several different alkali systems [40, 41, 42, 43, 44]. Recently Feshbach resonances between different alkali atoms have been observed [45, 46], leading to the possibility of polar molecules. The molecules produced are vibrationally excited. To get to absolute ground state molecules requires another technique such as the techniques developed for photo-association (PA). PA uses a laser to associate two colliding atoms into a molecule that has an excited electronic

state. Then, with the application of another laser, a stimulated Raman process can drive the excited molecule to the molecular ground state. PA has successfully been used to produce RbCs molecules in their absolute vibrational ground state [47, 48, 49]. KRb has also been photo-associated [50, 51], although not yet in its vibrational ground state. These indirect methods are currently confined to producing hetero-nuclear alkali molecules.

Another set of experimental techniques used to produce cold polar molecules are called direct methods, because they start with molecules and then cool them directly. There are many ways to do this, the first being buffer gas cooling [52, 53, 54, 55], that uses cold Helium to cool the molecules through collisions. Another successful means of cooling molecules is by electric-field-pulsed slowing or Stark slowing [56, 57, 58, 59, 60]. Other means of slowing molecules are light-field slowing [61], laser cooling [62], counter-rotating-nozzle slowing [63], single collision scattering [64], and beam skimming [65, 66]. The advantages of these techniques is that they are general enough to be used on almost any polar molecule or even non-polar molecules in some cases. These direct methods have been used to slow CaH, NH, OH, NH_3, and H_2CO, among others. The disadvantage is that direct methods have not achieved ultracold temperatures.

Regardless of the means by which molecules are cooled, it is necessary to understand the molecular interactions and how external fields can be used to influence them. With such an understanding, the dipolar interaction could be controlled and therefore the properties of the gas could be chosen. We now review the state of ultracold molecular collision theory.

1.2 A Review Ultracold Collision Physics

An area of rapid development in cold collision theory is in the understanding of the vibrational quenching of molecules. This research was motivated by the experimental production of Feshbach-associated molecules in highly excited vibrational states;

such processes are a first step toward understanding and accurately modeling ultracold chemical reactions [67, 68, 69, 70, 71, 72, 73, 74, 75, 76]. These studies focused on important issues such as the life time of vibrationally excited molecules in the presence of other molecules or atoms.

It might also be possible to control the chemical properties of ultracold molecules through various means such as external fields. An example would be the hydrogen abstraction process in $OH+H_2CO \rightarrow H_2O+HCO$, which by using electric fields could control intimate details of the chemical reaction [77]. The idea of sensitively controlling a chemical reaction could pave the way for detailed studies and significant advances in the understanding and observation of real time chemical reactions.

There have been a few theoretical studies on ultracold chemical reactions [78, 79, 80]. One particularly interesting study found that the chemical reaction $H_2 + F \rightarrow HF + H$ will still take place at significant rates even though the reaction has a barrier of 700 K [79]. Such studies show that studies of chemical reactions should be possible at ultracold temperatures. Later it was found that such large rates were resonance assisted [80], further bolstering the claim of control.

At the heart of all these studies is the two-body interaction of molecules that either make up the molecular gas or the reactants. Thus for an accurate theory of such systems, there must be a clear understanding of the two-body collision physics.

Some of the first studies explicitly dealing with ultracold collisions of molecules were those considering buffer-gas cooling and molecule-helium collisions [81, 82, 83, 84, 85]. Both were of great importance in understanding how the buffer gas system would affect the molecules to be cooled. These studies also explored the influence of the external magnetic field on the collisional properties of an ultracold gas as a means to control it. Since the success of these studies and the experimental achievement of cold trapped molecules, the attention of theorists has turned to the collisions of molecules.

There have been several studies of polar molecule-molecule collisions [86, 87, 88,

89, 90, 91, 92, 93] whose primary focus was the influence of external fields on the collisions. For a review, see Ref. [94]. One intriguing discovery has been the novel long-range scattering resonances dubbed "field-linked" states [90]. Field-linked states are produced when two weak-field seeking states collide and their dipolar interactions temporarily create a long-range bound state. Another proposed use of a magnetic field is to break weakly bound complexes [95]. Such studies have shown possible means of controlling collisions with external fields.

1.3 This Work

The focus of this thesis is to understand dipolar interactions of polar molecules in an ultracold environment. These studies are carried out through full quantum mechanical calculations exploring the collisions of two polar molecules and how external fields influence the collisions. This work was motivated by a desire to understand how to control the interaction of polar molecules. Such an understanding is increasingly paramount as experiments strive towards trapped ultracold polar molecules. Controlling the collisions of polar molecules could lead to a means to increase trap-life time or provide prescriptions for probing particular aspects of the dipolar gas one is interested in.

This theory will also facilitate many other theoretical studies and advance the broader understanding and applications of dipolar interactions. One avenue of contribution leads to the addition of realistic molecular interactions into many-body theories. In analogy with ultracold atoms, a clear understanding of the two-body interaction will be essential for the many-body theories to accurately describe and predict the collective behavior.

This work pursues an understanding of the long-range scattering properties of polar molecules and largely ignores the effects of short-range molecular interaction. There are two reasons for this omission: first, the surface that would govern such a

collision may not be well known and second, molecular scattering is largely determined by the long-range dipolar properties of the interaction. Thus many aspects of collisional control will originate from long-range scattering. Then as the experiments achieve colder temperatures, they will be able to systematically probe the short-range interaction with control already achieved by an understanding of the long-range scattering.

The order in which this thesis is presented is as follows: Chapter (2) reviews how molecules behave in the presence of external magnetic and electric fields, Chapter (3) reviews multichannel scattering theory and aspects of field dressing, Chapter (4) discusses how a magnetic field could be used to suppress inelastic losses in collisions of weak-field-seeking states of polar molecules [92]. Chapter (5) discusses how an electric field can be used to control collisions of strong-field-seeking states of polar molecules and identifies an intriguing set of scattering resonances found in this system [93].

Chapter 2

External Fields and Molecules

This chapter describes how external fields influence the internal states of molecules. To begin, we look at the Stark and Zeeman effects. We offer examples of Hund's case (a) and (b) molecules. The theory of how to treat asymmetric rigid rotors is also discussed. Then we look specifically at OH in the hyperfine basis and contrast the effects of electric and magnetic fields.

2.1 General Form of the Stark Effect

Since the electric field is a true vector (as opposed to a pseudovector), it only couples states of opposite parity [96]. For molecules, these states are usually separated in energy by an amount, which we will denote Δ. This means the Stark energies vary quadratically with low electric field and linearly only at higher fields once the Stark energy is greater than the splitting. This coupling of states of opposite parity is a general feature of the Stark effect, whether the electric field originates from an external source or from another molecule as in the dipolar interaction. In the following section we develop the Stark effect in a general manner to allow its results to be used in the dipolar interaction of rigid rotor molecules.

We assume that vibrational degrees of freedom are frozen out and the geometry of the molecule is constant. This is the rigid-rotor assumption that is justified at low temperatures because there is not enough energy to excite vibrational modes that are

usually several hundred Kelvin away in energy [97]. A molecular state is described in terms of the state vector $|JM_J\Omega\rangle$, where J is the molecule's rotational plus electronic angular momenta, M_J is the projection of J onto the lab axis, Ω is J's projection onto the molecular axis. We have suppressed the electronic degrees of freedom that are needed to specify the molecular state because they are spectators in the Stark effect at low fields and are constants of motion for our studies.

To describe the rigid rotor molecular wave function, we use $\langle\alpha,\beta,\gamma|JM_J\Omega\rangle = \sqrt{\frac{2J+1}{8\pi^2}}D^{J\star}_{M_J\Omega}(\alpha,\beta,\gamma)$, where α,β,γ are the Euler angles defining the molecular frame and $D^{J\star}_{M_J\Omega}$ is a Wigner D function (or rotation matrix). We use the short hand $\hat{\omega}$ to represent the Euler angles. For a complete discussion on the Wigner D function's properties see Refs. [97, 98, 99].

With this description of the molecular state, we can explore the basic properties of the Stark effect. The Stark Hamiltonian has the form

$$H_S = -\vec{\mu}\cdot\vec{\mathcal{E}}, \tag{2.1}$$

where $\vec{\mu}$ is the electric dipole moment of the molecule and $\vec{\mathcal{E}}$ is the electric field. We will take the field to be in the $\hat{z}$ direction of the fixed lab frame in subsequent chapters, but for the current discussion we pursue a general approach and allow the field to point in an arbitrary direction. The Stark interaction can be evaluated by decomposing the electric field into its spherical components and rotating the molecular dipole operator into the lab frame. To rotate an operator from the molecular frame, we again use a Wigner D function. In our case, the two frames are the lab and molecular frame, which are related by the same Euler angles $\hat{\omega}$ defining the molecular orientation. A rank k operator in the lab frame, T^k_q, can be expressed in terms of the molecular frame operators with the transformation: $T^k_q = \sum_\lambda D^{k\star}_{q\lambda}(\hat{\omega})T^k_\lambda$, where λ (q) is projection of the operator onto the molecular (lab) axes [97]. The inverse, a molecular frame operator described in terms of lab frame operators, is $T^k_\lambda = \sum_q D^k_{q\lambda}(\hat{\omega})T^k_q$.

The dipole is naturally defined in the molecular frame and most generally has the form $\vec{\mu} = \sum_k \mu_k \hat{e}_k$, but this is overkill. The dominant axis of symmetry ($\hat{e}_0$) usually has the only significant dipole moment because of symmetry. For example, a diatomic molecule has only one dipole moment [97]. For simple polyatomic molecules, there is generally only one component of the dipole moment that needs to be considered to get a physically realistic description. Thus the dipole moment has the form $\vec{\mu} = \mu \hat{e}_0$. The Stark Hamiltonian can be evaluated by rotating the dipole into the lab frame. Then in spherical coordinates, the Stark Hamiltonian has the form

$$H_S = -\sum_q \mathcal{E}_q D^{1\star}_{q0} \mu(\hat{\omega}). \tag{2.2}$$

To get a feel for what the Wigner D-function is, we note that $D^{1\star}_{q0}(\alpha, \beta, \gamma)$ is equal to $(-1)^{2q} C^1_q(\beta, \alpha)$, where C^1_q is a reduced spherical harmonic.

At the heart of evaluating the Stark effect, we find the field operator $D^{1\star}_{q0}$ coupling two molecular states, which themselves are described by D functions. Thus to evaluate the matrix element, we have an integral of three Wigner D-functions integrated over the molecular coordinates. Written out, the integral is

$$\begin{aligned} \langle J M_J \Omega | D^{1\star}_{q0}(\hat{\omega}) | J' M'_J \Omega \rangle &= \frac{[J, J']}{8\pi^2} \int d\hat{\omega} D^J_{M_J \Omega}(\hat{\omega}) D^{1\star}_{q0}(\hat{\omega}) D^{J'\star}_{M'_J \Omega}(\hat{\omega}) \\ &= [J, J'](-1)^{M_J - \Omega} \begin{pmatrix} J & 1 & J' \\ -M_J & q & M'_J \end{pmatrix} \begin{pmatrix} J & 1 & J' \\ -\Omega & 0 & \Omega' \end{pmatrix}. \end{aligned} \tag{2.3}$$

Here $\begin{pmatrix} \cdots \\ \cdots \end{pmatrix}$ is a 3-J symbol that describes the addition of two angular momenta. One of the properties of the 3-J symbol is that the bottom row must sum to zero to yield a nonzero result. This property tells us that $q = M_J - M'_J$ and $\Omega = \Omega'$, which is a partial statement of angular momentum conservation. We have also introduced the notation: $[j_1, j_2, ..., j_N] = \sqrt{(2j_1 + 1)(2j_2 + 1) \cdots (2j_N + 1)}$. With this matrix element, we are able to construct the Stark Effect for any rigid rotor molecule. For valuable discussions on the Stark effect, see Refs. [97, 100].

A molecule may have a nuclear spin that generates a hyperfine structure. Because of this, it is more appropriate to present the matrix elements in the hyperfine basis, where F and M_F define the state. Here F is the sum of J and the nuclear spin I in the usual angular momentum sense. Thus F can have the values ranging between $J+I$ and $|J-I|$. The energy separation between hyperfine levels is usually much less than either the rotational or Λ-doublet splitting between different parity states of the molecules.

We use the Wigner-Eckart theorem to compute the Stark matrix elements in a compact form. The matrix elements of the Stark effect are

$$\langle \alpha F M_F | H_S | \alpha' F' M'_F \rangle = -\mu \mathcal{E} \langle \alpha F M_F | D^{1\star}_{q0} | \alpha' F' M'_F \rangle, \tag{2.4}$$

which is written in terms of a purely geometrical matrix element. This geometrical matrix element can be evaluated with the application of the Wigner-Eckart Theorem

$$\begin{aligned} \langle \alpha F M_F | D^{1\star}_{q0} | F' M'_F \alpha' \rangle &= [F](-1)^{1+F'+M_F} \\ &\times \begin{pmatrix} F' & 1 & F \\ M'_F & q & -M_F \end{pmatrix} \langle \alpha F \parallel D^{1\star}_0 \parallel \alpha' F' \rangle. \end{aligned} \tag{2.5}$$

Here $\langle \alpha F \parallel D^{1\star}_0 \parallel \alpha' F' \rangle$ is the reduced matrix element, and α represents all remaining quantum numbers needed to uniquely determine the quantum state, such as Ω. We retained q as a place holder that takes on the appropriate value $M_F - M'_F$ when being evaluated. If we exploit the fact that the electric field is in the $\hat{z}$ direction, then $q = 0$, and we find that $M_F = M'_F$. We use the angular momentum conventions and statement of the Wigner-Eckart theorem defined by Brink and Satchler [98] that differ from other conventions like those used by Ref. [97].

A standard means of obtaining reduced matrix elements is by using the Wigner-Eckart Theorem on Eq. (2.3):

$$\begin{aligned} \langle \alpha J M | D^{1\star}_{q0} | \alpha' J' M'_J \rangle &= [J](-1)^{1+J'+M_J} \\ &\times \begin{pmatrix} J' & 1 & J \\ M'_J & q & -M_J \end{pmatrix} \langle \alpha J \parallel D^{k\star}_0 \parallel \alpha' J' \rangle. \end{aligned} \tag{2.6}$$

Then we set this result equal to the RHS of Eq. (2.3). From this equality, one can then solve for the reduced matrix element, which yields

$$\langle \alpha J \parallel D_0^{k\star} \parallel \alpha' J' \rangle = [J'](-1)^{-\Omega-J-2J'} \begin{pmatrix} J & 1 & J' \\ -\Omega & 0 & \Omega' \end{pmatrix}. \tag{2.7}$$

We now look into specific molecular examples and discuss the explicit basis sets used to describe molecules. When doing this, we maintain the use of hyperfine notation, but, at first, we offer simplified examples with $I = 0$. Then after we have illustrated the Stark effect, we closely study OH with hyperfine structure.

2.1.1 Molecular Examples: Hund's Case (b)

First, consider a Hund's case (b) molecule with $L = 0$. Hund's case (b) occurs when the electronic spin is decoupled from the molecular axis, but the orbital angular momentum is coupled to the molecular axis. Falling into this category are many molecules such as heteronuclear alkali dimers and SrO with $^{2S+1}\Sigma$ ground states. Here the parity of a state is identified by the quantum number J, $parity = (-1)^J$ [97]. The Stark effect therefore directly mixes the ground state, $J = 0$, with the first rotationally excited state, $J = 1$. Thus Δ, the energy splitting between the parity states, is $2B = BJ(J+1)$, where B is the rotational constant that is inversely proportional to the molecule's moment of inertia. The state is described simply by $|JM_J\rangle$.

Accounting for the possibility of nuclear spin and electronic spin, we produce general matrix elements in the hyperfine basis. Including the nuclear spin does not change the form of the Stark effect although the Stark effect can couple different hyperfine states together if they have the same M_F. In the hyperfine basis, we find the reduced matrix element to be

$$\begin{aligned} \langle \alpha F \parallel D_0^{1\star} \parallel F' \alpha' \rangle = {} & [N, N', J, J', F](-1)^{F+I++J+J'+S+N+N'} \\ & \times \begin{Bmatrix} F & F' & 1 \\ J' & J & I \end{Bmatrix} \begin{Bmatrix} J & J' & 1 \\ N' & N & S \end{Bmatrix} \begin{pmatrix} N' & 1 & N \\ 0 & 0 & 0 \end{pmatrix}, \end{aligned} \tag{2.8}$$

where the index α represents N, S and $\{\cdots\}$ is a 6-J symbol that describes the addition of three angular momenta. We are able to relate reduced matrix elements in the F basis to reduced matrix elements in the J basis through relations given in Brink and Satchler [98]. The one used for the current discussion is of the form:

$$\langle \alpha(JI)F \parallel D_0^{1\star} \parallel \alpha'(J'I')F' \rangle \propto \left\{ \begin{array}{ccc} F & F' & 1 \\ J' & J & I \end{array} \right\} \langle \alpha J \parallel D_0^{1\star} \parallel \alpha' J' \rangle \delta_{II'}. \tag{2.9}$$

Here operator $D_0^{1\star}$ does not act on I, and therefore it is left unchanged by the operator. However, it does act on J, and by decomposing F into J and I with some angular momentum algebra, which results in the 6-J symbol, we are able to obtain the reduced matrix element in the J basis.

As an example of this system, we pick RbCs, which has a $^1\Sigma$ ground state. Since it is a singlet state, $J = N$. We have plotted the Stark effect for RbCs in Fig. 2.1. In this plot, we have also assumed that I is zero. A common feature of the Stark effect is that states with the same M_J repel each other. For example, this can be seen by looking at the $|JM_J\rangle = |00\rangle$ and $|10\rangle$. These states are coupled and repel each other. For this reason the $|00\rangle$ state, which goes down in energy, is deemed a strong-field seeker, and the $|10\rangle$ is a weak-field seeker (at small field). One other feature of the Stark effect worth noting is the degeneracy between the values of $\pm M$. This degeneracy explains why $J = 1$ has only two curves, one for $M_J = 0$ and the other for $|M_J| = 1$.

2.1.2 Hund's Case (a)

Now consider a Hund's case (a) molecule with $\Omega \neq 0$. Hund's case (a) occurs when the electronic spin and orbital angular momentum are strongly coupled to the molecular axis. A good example of this case is the OH radical, which has a ground state of $^2\Pi_{3/2}$. In addition to being a Π state, this molecule has a pair of nearly degenerate states with $\Lambda = \pm 1$, where Λ is the projection of the orbital angular momentum onto the molecular axis. The energy eigenstates of such a molecule in zero electric field are

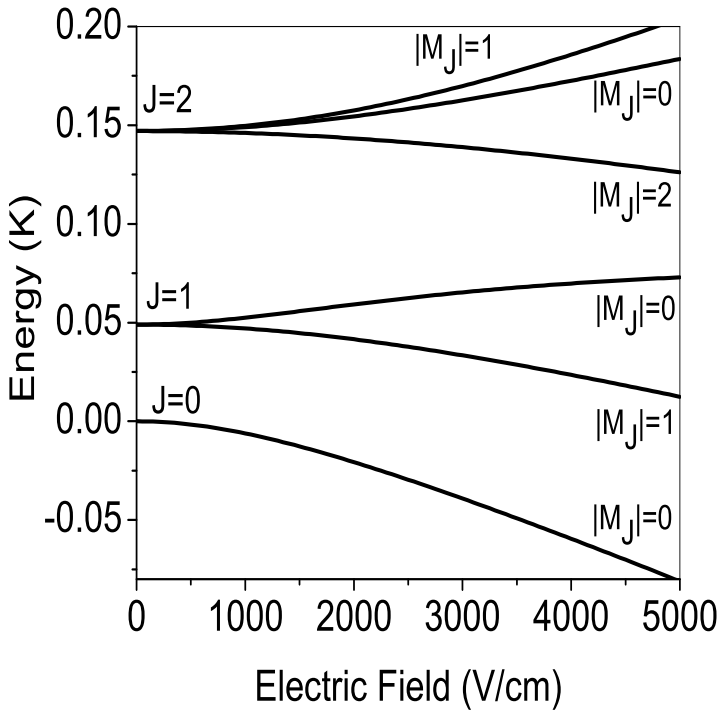

Figure 2.1: The Stark effect in RbCs, which has a $^1\Sigma$ ground state. The Stark effect couples different rotational levels but preserves $|M_J|$. We have used B=0.0245 (K) and μ=1.3 (D) [49].

eigenstates of parity, $|JM_J\bar{\Omega}\epsilon\rangle$, where $\epsilon = +(-)$ represents the e (f) lower (upper) parity state of the doublet and $\bar{\Omega} = |\Omega|$. The parity of this molecule is $\epsilon(-1)^{J-1/2}$; for details see Refs. [92, 100]. The parity basis is written

$$|JM_J\bar{\Omega}\pm\rangle = \left(\frac{|JM_J\Omega\rangle + \epsilon|JM_J - \Omega\rangle}{\sqrt{2}}\right). \tag{2.10}$$

In the parity basis, there is no dipole moment, because this basis is a linear combination of electric dipole "up" and "down." This fact has important implications for the dipole-dipole interaction. In the parity basis, the energy splitting between the different parity states (e/f) is called the Λ-doublet. The Λ-doublet arises from a coupling to a nearby Σ state. It is the coupling of the Σ state to Π state of the same parity that breaks the degeneracy of the two Π parity states [97].

In this discussion, we explicitly take the field to be in the $\hat{z}$ direction. In the rigid rotor basis Ω has a definite sign, and the matrix elements are well known [102]:

$$\langle JM_J\Omega|H_S|JM_J\Omega\rangle = \frac{-\mu\mathcal{E}\Omega M_J}{J(J+1)}. \tag{2.11}$$

In the Stark effect, there is a degeneracy between states with the same sign of ΩM_J, meaning $\pm M_J$ are degenerate in an electric field. We can recast the Stark Hamiltonian into the J-parity basis set from Eq. (2.10). Doing so, we find

$$\langle JM_J\bar{\Omega}\epsilon|H_S|JM_J\bar{\Omega}\epsilon'\rangle = \frac{-\mu\mathcal{E}\bar{\Omega}M_J}{J(J+1)}\left(\frac{1-\epsilon\epsilon'}{2}\right). \tag{2.12}$$

In this expression, the factor $(1-\epsilon\epsilon')/2$ explicitly represents the electric field coupling between states of opposite parity, since it vanishes for $\epsilon = \epsilon'$.

We have plotted the Stark effect for OH in Fig. 2.2, and we have ignored the next rotational state because it is over 80 (K) away. We have assumed that $J = \bar{\Omega} = 3/2$ and $I = 0$. Again we see the strong- (f) and weak- (e) field seeking states. In fact, the labels $e(f)$ are reserved for the lower (upper) set of states in a Λ-doublet. So in general, e is usually a weak-field seeker. A weak-field seeker is a molecular state whose internal energy increases as an external field increases.

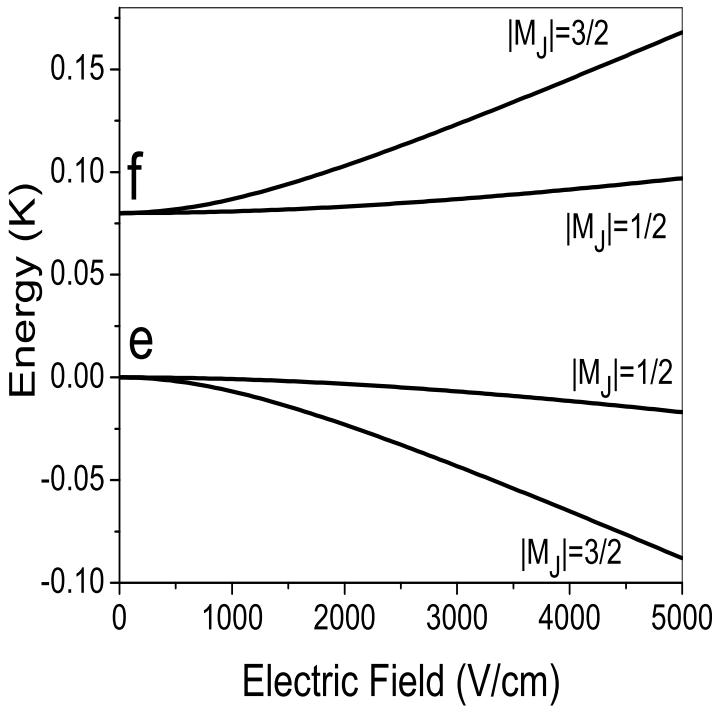

Figure 2.2: The Stark effect for OH excluding hyperfine structure, with its $^2\Pi_{3/2}$ ground state. We have set the Λ-doublet energy equal to 0.08 (K) and electric dipole of $\mu =$ 1.668 (D) [87]. One key feature of this plot is that at low field, the energies vary quadratically and then vary linearly at high field once the Stark energy is larger than the splitting. This transition happens at roughly 1000 (V/cm) for OH [87].

To get a feel for this matrix element, we need to understand in which direction the dipole points or the orientation of the molecular axis (from O to H). We can first determine M_J, but this is not enough because J can be either aligned or anti-aligned with the molecular axis (+ or $-\Omega$). Thus we also need to know the signed values Ω. With the combination $M_J\Omega$, we can determine the dipole orientation. This is why there is a degeneracy between $\pm M$ because for $M_J\Omega > 0$, we find the dipole is oriented along $\hat{z}$ and for $M_J\Omega < 0$, we find the dipole is oriented against $\hat{z}$.

Including the hyperfine structure we find the reduced matrix element to be

$$\langle \alpha F \parallel D_0^{1\star} \parallel F'\alpha' \rangle = (-)^{1+I+F+J+J'-\bar{\Omega}}[F', J, J'] \begin{Bmatrix} F & F' & 1 \\ J' & J & I \end{Bmatrix} \begin{pmatrix} J' & 1 & J \\ -\bar{\Omega} & 0 & \bar{\Omega} \end{pmatrix} \left(\frac{1 + \epsilon\epsilon'(-1)^{J+J'+2\bar{\Omega}+1}}{2} \right). \tag{2.13}$$

Here the index α represents $\epsilon, \bar{\Omega}$, and J.

2.1.3 Asymmetric Rotors

To extend this formalism to include asymmetric rotors, there is the additional step of including the rotational Hamiltonian that mixes Ω in constructing the molecular eigenstates. For an asymmetric rotor, there are three distinct moments of inertia and therefore three distinct rotational constants. The rotational Hamiltonian is $H_{rot} = A\mathbf{J}_a^2 + B\mathbf{J}_b^2 + C\mathbf{J}_c^2$, where the rotational constants are labeled so that $A > B > C$ and a, b, and c are the axis labels in the molecular frame. This additional structure mixes Ω such that it is no longer a good quantum number. This implies that we need to diagonalize the rotational Hamiltonian to get the molecular eigenstates in addition to the Stark Hamiltonian if such a field is present.

To describe an asymmetric rotor, we first define Ray's asymmetry parameter κ,

body fixed axis	I	II	III
x	b	c	a
y	c	a	b
z	a	b	c

Table 2.1: Correspondence of principal axes to the molecular axes for different limits of κ[101].

which defines the shape of the asymmetric rotor [101]:

$$\kappa = \frac{2B - A - C}{A - C}. \tag{2.14}$$

This parameter describes the geometry of the molecule as it ranges between the symmetric top limits. In the prolate limit (cigar) we have $B = C$, and thus κ = -1. Whereas in the oblate limit (pancake), we have $A = B$, and thus $\kappa = 1$.

As the molecular geometry changes with varying κ, so does the way in which the rotational Hamiltonian is best described. To describe a given molecule, we must assign axis labels (a, b, c) to the molecular frame (x, y, z). For different limits of κ, we define different cases of axes assignment. For $\kappa = -1$, we use case I, which assigns the a axis to the molecular z axis. When $\kappa = 0$, we use case II, which assigns b to z. Finally for $\kappa = 1$, we use case III, which assigns c to z. The complete list of axes correspondence are in Table 2.1, which is adapted from Ref. [101].

There is a standard way to write down the rotational Hamiltonian for an asymmetric rotor taking advantage of molecular symmetries. We now present this methodology. A more complete discussion is given in Refs. [101, 99]. First we rewrite the rotational Hamiltonian as

$$H_{rot} = \frac{A + C}{2}\mathbf{J}^2 + \frac{A - C}{2}H(\kappa), \tag{2.15}$$

where

$$H(\kappa) = \mathbf{J}_a^2 + \kappa\mathbf{J}_b^2 - \mathbf{J}_c^2. \tag{2.16}$$

Parameter	I	II	III
F	(κ-1)/2	0	(κ+1)/2
G	1	κ	-1
H	-(κ+1)/2	1	(κ-1)/2

Table 2.2: Parameters F,G, and H that are part of $H(\kappa)$ [101].

The matrix elements of $H(\kappa)$ are:

$$\langle JM\Omega|H(\kappa)|JM\Omega\rangle = F(J(J+1)-\Omega^2)+G\Omega^2$$

$$\langle JM\Omega\pm 2|H(\kappa)|JM\Omega\rangle = Hf(J,\Omega\pm 1)^{1/2}$$

$$f(J,\Omega\pm 1)=\frac{1}{4}\{J(J+1)-\Omega(\Omega\pm 1)\}\{J(J+1)-\Omega(\Omega\pm 1)\Omega(\Omega\pm 2)\}. \quad (2.17)$$

The second equation is off-diagonal in Ω; it is nonzero only if $\Omega' = \Omega\pm 2$. The parameters F, G, and H are case dependent and specified in Table 2.2.

The zero-field eigenvalues and molecular eigenstates are achieved by diagonalizing Eq. (2.15). The eigenvalues have the form

$$E(J_\tau M) = \frac{A+C}{2}J(J+1)+\frac{A-C}{2}E(\kappa). \quad (2.18)$$

Here $E(\kappa)$ are the eigenvalues of $H(\kappa)$. We have used a standard labeling scheme for the asymmetric rotor's eigenstates, $|J_\tau M\rangle$, where τ is the phenomenological quantum number taking the place of Ω. For a given J and M, τ starts at $-J$ for the lowest energy state and ends with J for the highest rotational state, for a total of $2J+1$ states for a given value of J and M.

To get field molecular eigenstates in a field, one must diagonalize the rotational Hamiltonian described above in the rigid rotor basis (Eq. 2.15) together with the Stark Hamiltonian in Eqs. (2.4) and (2.8).

To illustrate the rotationally excited spectrum of an asymmetric rotor in an electric field, we picked formaldehyde (H_2CO) as an example. This example is in Fig. 2.3. Its rotational constants are $A = 13.558$, $B = 1.867$, and $C = 1.675$ (K), yielding $\kappa = -0.96$, and identifying this molecule as being in the prolate limit. Its electric dipole

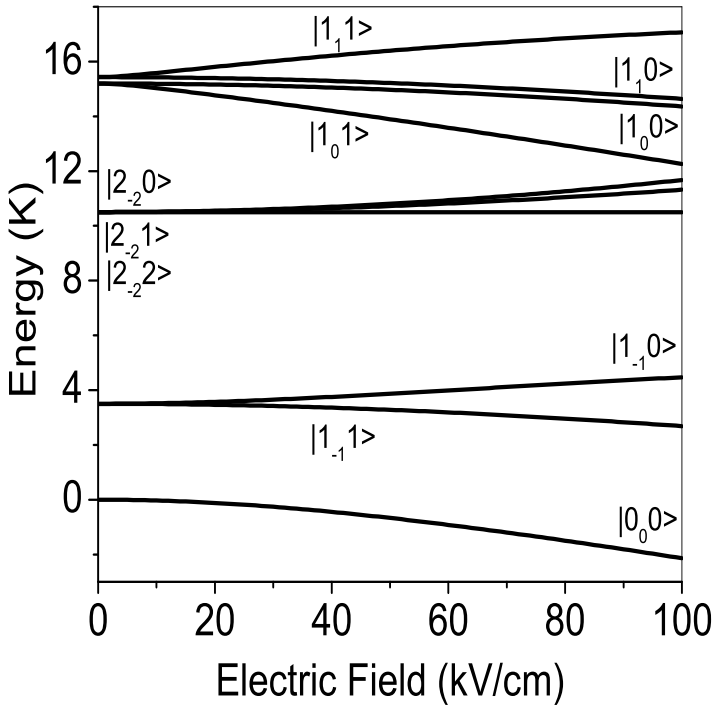

Figure 2.3: This is the Stark effect in formaldehyde, H_2CO. The states are labeled with the usual asymmetric rotor notation $|J_\tau M_J\rangle$.

moment is 2.34 (D) [101]. For ultracold collisions, the main deviation of this example from other symmetric rigid rotors is that the rotationally excited states are ordered differently than a symmetric rotor. Furthermore, some rotationally excited states have different zero-field basis sets. Figure 2.3 shows some $J = 2$ states are lower in energy than some $J = 1$ rotationally excited states.

2.1.4 The Zeeman Effect

The effect of the magnetic field can be treated in much the same way as the effect of an electric field. The Stark and Zeeman effects in molecules have a similar form, since both arise as the scalar product of a dipole moment with an external field. Their influence on the molecule is quite different, however, since they act on fundamentally different degrees of freedom. The electric field is concerned primarily with where the charges *are* in the molecule, whereas the magnetic field is concerned with where they are *going*. This is of paramount importance, since it implies that the electric field is a true vector (odd under the parity operation), whereas the magnetic field is a pseudovector (even under parity) [96]. This means that the magnetic field respects parity. Furthermore, there are diagonal contributions that directly shift molecular energy levels.

The vector form of the Zeeman effect is

$$H_Z = -\vec{\mu}_B \cdot \vec{B} = \mu_0(g_e\vec{S} + g_L\vec{L}) \cdot \vec{B}. \tag{2.19}$$

Here μ_0 is the Bohr magneton, g_e is the electron's g factor ($g_e \sim 2.002$), $g_L = 1$, and $\vec{S}$ and $\vec{L}$ are the spin and orbital angular momentum vectors of the electron. We use atomic units, so $\hbar = 1$. We assume that the magnetic field is in the laboratory-fixed $\hat{z}$ direction. There are other contributing terms, but they are smaller by roughly a factor of 10^{-3} [97]. The magnetic field's interaction with the molecule is diagonal in parity, and it has the ability to shift and possibly separate energy eigenstates of the molecule.

The Zeeman Hamiltonian can be treated in a parallel manner to the Stark Hamil-

tonian by using the Wigner Eckart theorem to decompose it into molecule and case dependent reduced matrix elements. Then the matrix elements of Eq. (2.19) have the form

$$H_Z = -\mu_B B[F](-1)^{1+F'+M_F} \begin{pmatrix} F' & 1 & F \\ M'_F & 0 & -M_F \end{pmatrix} \langle \alpha F \parallel D_0^{1\star} \parallel \alpha' F' \rangle. \tag{2.20}$$

We have suppressed the electronic degrees of freedom because they are constants of the motion, but now we need to know their form. The different Hund's cases are the way in which the electronic structure is categorized. We now discuss the Zeeman effect for Hund's cases (a) and (b).

In Hund's case (b) with $L = 0$, the electronic spin degrees of freedom are described most accurately in the lab frame. This means that the spin angular momenta operator is $|SM_S\rangle$, which is embedded in $|JM_J\rangle$. This implies that there is no rotation needed to evaluate the Hamiltonian. Thus the Zeeman Hamiltonian becomes $\mu_0 g_e S_z B_z$, with matrix elements proportional to $\mu_0 g_e M_S B$. Thus to understand the magnetic field's effect, we must decompose the quantum number F into J+I and J into S+N to evaluate the reduced matrix element. For the Hund's case (b) molecule, we find the reduced matrix element to be

$$\begin{aligned} \langle \alpha F \parallel \vec{\mu}_B D_0^{1\star}(\hat{\mu}_B) \parallel \alpha' F' \rangle = \mu_0 [S, J, J', F'](-1)^{I+F+J+J'+N+S} \\ \times \begin{Bmatrix} F & F' & 1 \\ J' & J & I \end{Bmatrix} \begin{Bmatrix} J & J' & 1 \\ S' & S & N \end{Bmatrix} \sqrt{S(S+1)}. \end{aligned} \tag{2.21}$$

In Hund's case (a), the electronic degrees of freedom are accurately represented by the state vector $|S\Sigma\rangle|L\Lambda\rangle$, where Σ (Λ) is the projection of the electronic spin (orbital angular momentum) onto the molecular axis. Thus to evaluate the matrix element, we need to rotate the dipole operators into the lab frame. The Zeeman Hamiltonian matrix elements are therefore proportional to $\mu_0 B(g_e\Sigma + g_L\Lambda)$. In the J basis, the

Zeeman Hamiltonian takes the form [103]

$$\langle JM_J\Omega|H_Z|JM_J\Omega\rangle = \frac{\mu_0 B(\Lambda + g_e\Sigma)\Omega M_J}{J(J+1)}. \tag{2.22}$$

This is quite similar to the equivalent expression (2.11) for the Stark effect, except that the electron's g-factor plays a role. Interestingly, for a $^2\Pi$ state, the prefactor $(\Lambda+g_e\Sigma)\Omega$ is always greater than zero. We now recast the Zeeman interaction into the J-parity basis set (2.10). This gives us

$$\langle JM_J\bar{\Omega}\epsilon|H_Z|JM_J\bar{\Omega}\epsilon'\rangle = \frac{\mu_0 B\left(\bar{\Lambda} + g_e\bar{\Sigma}\right)\bar{\Omega}M_J}{J(J+1)}\delta_{\epsilon\epsilon'} \tag{2.23}$$

for $\bar{\Omega} = \bar{\Lambda} + \bar{\Sigma}$ states. Here we have use $\bar{\Lambda}$ to denote $|\Lambda|$, likewise for $\bar{\Sigma}$.

It is worth that noting if $\bar{\Omega} = 1/2$ for a $^2\Pi_{3/2}$ molecule, such as OH, then the Zeeman matrix element is

$$\langle JM_J\bar{\Omega}\epsilon|H_Z|JM_J\bar{\Omega}\epsilon'\rangle = \frac{\mu_0 B\left(\bar{\Lambda} - g_e\bar{\Sigma}\right)\bar{\Omega}M_J}{J(J+1)}\delta_{\epsilon\epsilon'}. \tag{2.24}$$

Here the orbital and spin contributions to the molecular magnetic moment nearly cancel, to within the deviation of $g_e/2$ from one.

The key feature of the Zeeman matrix element (2.23) is that it is diagonal in ϵ, in contrast to the Stark matrix element. The full matrix element including hyperfine structure is

$$\langle \alpha F \parallel \vec{\mu}_B D_0^{1\star}(\hat{\mu}_B) \parallel F'\alpha'\rangle = [J, J', F'](-1)^{1+J+J'+I+F-\bar{\Omega}}$$
$$\times\mu_0(\bar{\Lambda} + g_e\bar{\Sigma})\left(\frac{1+\epsilon\epsilon'(-1)^{J+J'+2\bar{\Omega}}}{2}\right)\begin{Bmatrix} F & F' & 1 \\ J' & J & I \end{Bmatrix}\begin{pmatrix} J & 1 & J' \\ -\bar{\Omega} & 0 & \bar{\Omega} \end{pmatrix}. \tag{2.25}$$

For the OH ground state where $J = 3/2 = \bar{\Omega}$, an important feature of this interaction is $1 + \epsilon\epsilon'(-1)^{J+J'+2\bar{\Omega}}$ reduces to $\delta_{\epsilon\epsilon'}$. For a complete discussion on the Zeeman effect in molecules, see Ref. [97].

2.2 Electric versus Magnetic Fields

We now directly contrast the effect of electric and magnetic fields in OH and focus on two features that can be exploited in collisions. First, the electric field couples to states of opposite parity and polarizes the molecules as the electric field is increased. Second, the magnetic field directly changes the energy levels of molecular states and respects parity.

Relevant molecular energy scales for OH in this scattering problem are the Λ-doublet splitting that is $\Delta \sim 0.0797$ K, and the hyperfine splitting is $\Delta_{hf} \sim 0.0038$ K. OH also has an electric dipole moment that is $\mu \sim 1.668$ D.

2.2.1 Stark Effect in OH with Hyperfine Structure

The distinguishing feature of the Stark effect is that it mixes molecular states of opposite parity separated by the Λ doublet splitting. A consequence of this is that the Stark energies vary quadratically with electric field at low fields and linearly only at higher fields. The field where this transition occurs is given roughly by equating the field's effect $\vec{\mu} \cdot \vec{\mathcal{E}}$ to the Λ doublet splitting. In OH, this field is approximately $\mathcal{E}_0 \sim \Delta/\mu \sim 1000(V/cm)$ [87].

Finally, using Eq. (2.5) and (2.13), we arrive at the working matrix elements of the Stark effect:

$$\begin{aligned}\langle F M_F \epsilon | H_S | F' M_F \epsilon' \rangle = -\mu\mathcal{E} \left(\frac{1 + \epsilon\epsilon'(-1)^{J+J'+2\bar{\Omega}+1}}{2} \right) \\ \times (-1)^{J+J'+F+F'+I+M_F-\bar{\Omega}} [F, F', J, J'] \\ \times \begin{pmatrix} J' & 1 & J \\ -\bar{\Omega} & 0 & \bar{\Omega} \end{pmatrix} \begin{pmatrix} F' & 1 & F \\ M_F & 0 & -M_F \end{pmatrix} \begin{Bmatrix} F & F' & 1 \\ J' & J & I \end{Bmatrix}. \end{aligned} \tag{2.26}$$

Figure 2.4 shows the energy levels of OH in the presence of an electric field. Both parity states are shown, labeled e and f. An essential point of Fig. 2.4 is that the e and f states repel as the electric field is increased. This means that all of the f (e) states

increase (decrease) in energy as the field in increased, implying that states of the same parity stay close together in energy as the field is increased. This fact has a crucial effect on inelastic scattering, as we will show.

The highest-energy state in Fig. 2.4 is the stretched state with quantum numbers $|FM_F\epsilon\rangle = |22-\rangle$. It is this state whose cold collisions we are most interested in, because (i) it is weak-field seeking and (ii) collisions at low temperature result almost entirely from long-range dipole-dipole interactions [87].

2.2.2 Zeeman Effect in OH with Hyperfine Structure

The Zeeman effect respects parity and this gives rise to a very different result when an external field is applied. Using Eq. (2.20) and (2.25), we find the matrix elements are

$$\begin{aligned}
&\langle FM_F\epsilon|H_Z|F'M_F\epsilon'\rangle = \\
&\mu_0 B(\bar{\Lambda}+g_e\bar{\Sigma})\left(\frac{1+\epsilon\epsilon'(-1)^{J+J'+2\bar{\Omega}}}{2}\right) \\
&\times(-1)^{J+J'+F+F'+I+M_F-\bar{\Omega}}[F,F',J,J'] \\
&\times\begin{pmatrix} J & 1 & J' \\ -\bar{\Omega} & 0 & \bar{\Omega}' \end{pmatrix}\begin{pmatrix} F' & 1 & F \\ M_F & 0 & -M_F \end{pmatrix}\begin{Bmatrix} F & F' & 1 \\ J' & J & I \end{Bmatrix}.
\end{aligned} \tag{2.27}$$

Figure 2.5 shows the Zeeman energies in the hyperfine basis, for low [Fig. 2.5(a)] and high [Fig. 2.5(b)] fields. For OH in the $^2\Pi_{3/2}$ state, the parity factor $\left(\frac{1+\epsilon\epsilon'(-1)^{(J+J'+2\bar{\Omega})}}{2}\right)$ reduces simply to $\delta_{\epsilon\epsilon'}$. Because the magnetic field preserves parity, Fig. 2.5 (b) amounts to two copies of the same energy level diagram, separated in energy by the lambda doublet energy. For small magnetic fields, the molecular g-factor is $g_{mag}^{OH} \propto (F^2+J^2-I^2)$ and is always positive for OH. This is in contrast to the low-field magnetic moment of alkali atoms that is $g_{mag}^{alkali} \propto (F^2-J^2-I^2)$ (and where J, of course, refers to the sum of orbital and spin angular momenta). In Eq. (2.27) for $\bar{\Omega}=1/2$, the factor $\bar{\Lambda}+g_e\bar{\Sigma}$ goes to $\bar{\Lambda}-g_e\bar{\Sigma}$.

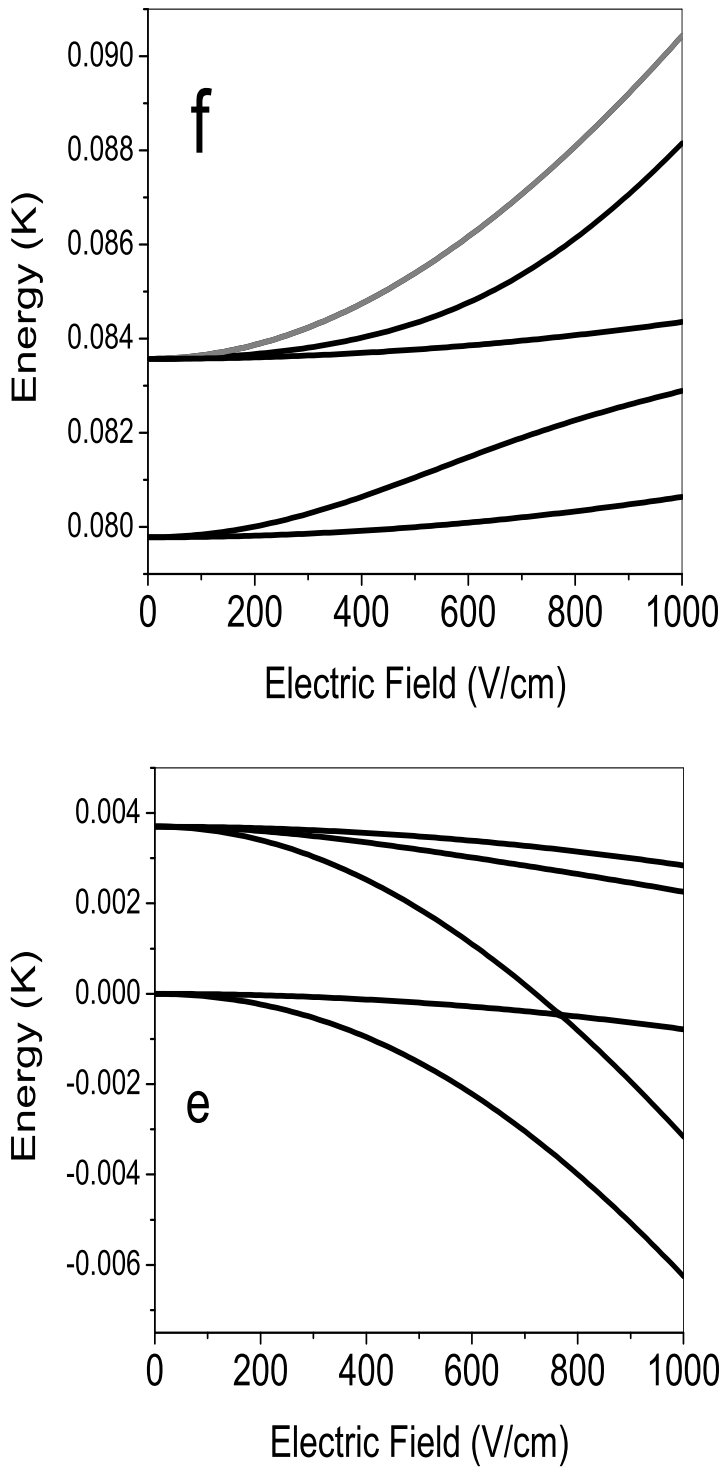

Figure 2.4: Stark effect for the ground state of OH with the hyperfine structure accounted for. In zero field, the f and e states are separated by the Λ-doublet energy. The gray line indicates the state of interest for our analysis, the $|22-\rangle$ state. An important feature of this interaction is that the opposite parity states repel, and thus like parity states stay close together in energy.

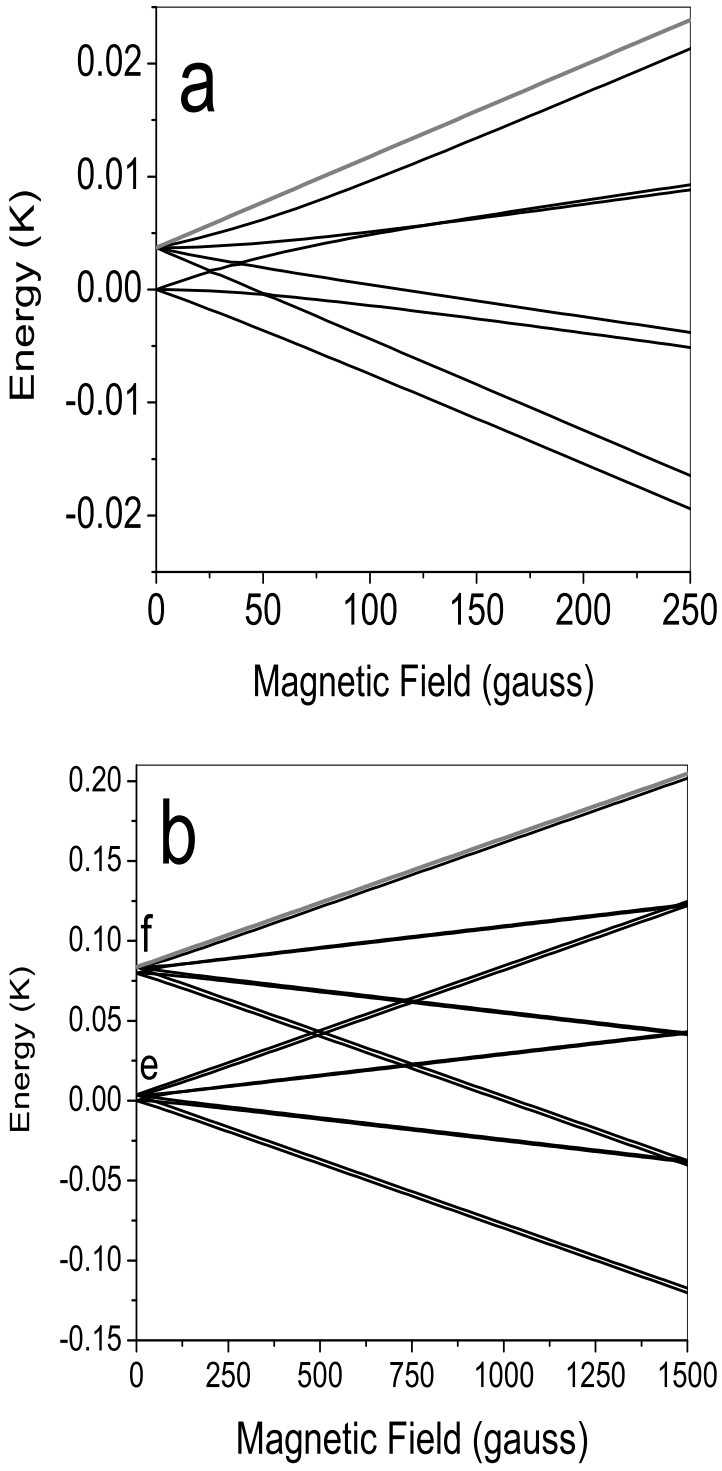

Figure 2.5: Zeeman effect for the ground state of OH, in low (a) and high (b) fields. This plot is the same for both the e and f states for zero electric field because the Zeeman interaction preserves parity. The $|22-\rangle$ state is indicated in gray.

It is important to directly contrast the effects of the external fields for the examples given here. First, the Stark effect polarized the molecule by mixing the parity states; therefore all of the f states increase in energy while all of the e states decrease as the electric field is increased, as shown in Fig. 2.4. This results in the weak-field seeking molecular states remaining relatively close together in energy as the field is increased. This is important for inelastic collisions, which will be discussed in Chapt. 4.

The behavior of the molecular states in a magnetic field is dramatically different. First, parity is a conserved. Second, the Zeeman energy depends on the M quantum number, this as seen in the matrix element given in Eq. (2.23). These two facts imply states of a given parity will separate in energy as the field is increased; this is seen in Figs. 2.5 (a) and (b). This result can be used to suppress inelastic collisions, it will also be discussed in Chapt. 4.

Chapter 3

Two-Body Multichannel Scattering Theory

This chapter outlines multichannel scattering theory, field dressing, the dipole-dipole interaction, the Born approximation, and adiabatic representation.

The theory of two-body scattering is a mature and established field; therefore we only provide an overview of scattering theory as needed for our studies of molecular collisions. For a complete development of scattering theory see Refs. [104, 105]. To study collisions of two molecules, we will start with the time-independent Schrödinger equation (TISE):

$$H|\Psi\rangle = E|\Psi\rangle. \tag{3.1}$$

Here H is the total Hamiltonian describing the system, E is energy eigenvalue, and $|\Psi\rangle$ is the quantum state of the two molecules whose interaction we are interested in. To solve this problem, we use coordinates describing the center of mass ($\vec{R}_m$) and relative coordinate ($\vec{R}$). We solve Eq. (3.1) in free space, so the this coordinate system leads to an uncoupled set of equations. For our purposes of studying molecular collisions, the TISE governing the relative motion of the molecules has the form

$$\left(\underline{T} + \underline{V}(\mathbf{R}) + \underline{H}_{int}\right)|\Psi\rangle = E|\Psi\rangle. \tag{3.2}$$

The terms in the Hamiltonian are the kinetic energy ($\underline{T}$) and molecular interaction ($\underline{V}$). $\underline{H}_{int}$ describes the internal energy and the interaction with any external fields for each molecule. We treat the effect of the external fields in perturbation theory and assume

it is independent of R. The underlined operators indicate they are matrices, implying Eq. (3.2) is actually a set of coupled equations. There is an equation for each unique pair of molecular states needed to describe the molecular dynamics. We now discuss the asymptotic form of Eq. (3.2) and how to extract physical information from boundary conditions.

3.1 Multichannel Formalism

The need for multichannel formalism originates from the internal structure of molecules. For example, different molecular states have distinct behavior in an external field, as do their pairwise interactions. This makes it necessary to account for molecular structure, to achieve an accurate model of the molecular interaction. To understand how these internal degrees of freedom enrich scattering, we write the wavefunction in terms of an incident plane wave and scattered spherical waves. For the multichannel scattering problem, the wavefunction is

$$\langle \vec{R}|\Psi^{(m)}\rangle = e^{\vec{i}k_m\cdot\vec{R}}|\chi_m\rangle + \sum_n \frac{e^{ik_nR}}{R} f_n^{(m)}(\theta,\phi)|\chi_n\rangle. \tag{3.3}$$

Here we have introduced χ_m, which represents the internal state of both molecules, including all internal molecular degrees of freedom. The scattering amplitude $f_n^{(m)}(\theta,\phi)$ depends on the incident (m) and final state (n) of the molecules. This implies that a scattering event can change the internal states of the molecules. If the molecular state changes, i.e., $m \neq n$, then the collision is deemed inelastic. If the molecular state is unchanged by the collisions, it is called elastic.

To account for the relative angular degrees of freedom we expand the $\vec{R}$ dependent wavefunction in terms of spherical harmonics, this is the partial wave expansion. The spherical harmonics account for the orbital motion of the colliding molecular pair.

We form unique combinations of spherical harmonics and molecular pairs called *channels* to expand the wavefunction in. For example, if we have molecules with two

internal states, say $|\uparrow\rangle$ and $|\downarrow\rangle$, then the molecular scattering states $|\chi_n\rangle$ could be $|\uparrow_1\uparrow_2\rangle$, $|\downarrow_1\uparrow_2\rangle$, $|\uparrow_1\downarrow_2\rangle$, and $|\downarrow_1\downarrow_2\rangle$. To construct channels, we also need to factor in the partial wave component. This results in a channel, $|f\rangle$, being defined by the quantum states, $|\chi_{n_f}\rangle|l_f m_{l_f}\rangle$, where $\langle\theta\phi|l_f m_{l_f}\rangle = Y_{l_f m_{l_f}}(\theta,\phi)$ is a spherical harmonic. In this example, a few possible channels are $|\uparrow_1\uparrow_2\rangle|00\rangle$, $|\uparrow_1\uparrow_2\rangle|20\rangle$, or $|\downarrow_1\uparrow_2\rangle|42\rangle$. Another notation we use when denoting the scattering basis is $|12lm_l\rangle$, where the $|12\rangle = |\chi_n\rangle$ or $|1\rangle$ ($|2\rangle$) denotes all of the quantum numbers needed to define the first (second) molecule.

We expand the wavefunction in channels, i.e.

$$\langle\vec{R}|\Psi^{(i)}\rangle = \sum_f \frac{1}{R}\psi_f^{(i)}(R)Y_{l_f m_{l_f}}(\theta,\phi)|\chi_{n_f}\rangle. \tag{3.4}$$

Here $\psi_f^{(i)}$ is a radial wavefunction for the f^{th} channel, of the i^{th} solution to Eq. (3.2). In this expansion, we have included a factor of R^{-1} to eliminate the first derivative in the radial coordinate of the radial TISE. The channel index, f, denotes all of the quantum numbers, including the partial wave number, l_f and m_{l_f} and quantum numbers for the two molecular states, n_f.

Furthermore, we pick the molecular states (or linear combinations of them) such that they diagonalize H_{int}, which can lead to different thresholds. This implies channels can have different wave numbers, i.e., $k_f = \sqrt{2m_r(E-E_f)}$, where $H_{int}\chi_{n_f} = E_j\chi_{n_f}$ and m_r is the reduced mass. Here E_j defines the threshold for a given set of molecular states. This choice of states is called "field dressed" if there is an external field, which will be discussed later. We adopt a shorthand, $Y_{l_j m_{l_f}}(\hat{R})\chi_{n_f} = \phi_f$, that describes all of the channel's quantum numbers except the radial coordinate.

By expanding the wavefunction, Eq. (3.4), and by multiplying by ϕ_f on the left and integrating over these degrees of freedom, we can reduce Eq. (3.2) into a set of

coupled equations describing the interaction of the molecules. These equations are

$$\sum_f \left(\left(\frac{-\hbar^2}{2m_r} \frac{d^2}{dR^2} + \frac{\hbar^2 l_f(l_f+1)}{2m_r R^2} - E + E_f \right) \delta_{fi} + V_{fi}(\vec{R}) \right) \psi_f^{(i)}(R) = 0. \tag{3.5}$$

The intermolecular potential $V_{fi}(\vec{R})$ is $\langle \phi_f | V(\vec{R}) | \phi_i \rangle$, which has averaged over all coordinates other than R. Thus it contains all of the information about the molecular interaction. δ_{fi} is a Kronecker delta which has the value of 1 if $i = f$ or zero otherwise. m_r is the reduced mass of the system. We make the association that the i^{th} solution has the i^{th} channel as the incident channel.

In principle, this infinite set of equations must be simultaneously solved. However this is a few too many equations to actually solve numerically. So to solve the system, we need to converge any given calculation with respect to a number of partial waves and a number of molecular states included in a calculation. For ultracold collisions, few partial waves are actually needed because at low energy, the centrifugal barrier, the $l_f(l_f+1)$ term in Eq. 3.5, suppresses the effect of scattering with large l. However, cold collisions of dipolar objects are subtle and require careful attention.

We need to apply boundary conditions to get a physically meaningful solution to Eq. (3.5). The first boundary condition is to demand that all solutions be zero at $R = 0$:

$$\psi^{(i)}(0) = 0. \tag{3.6}$$

This boundary demands that the wavefunction be finite at $R = 0$. The next boundary condition is applied at large R, where $V_{fi} \to 0$. It is this condition that allows us to extract the scattering information from the solutions to Eq. (3.5). This boundary condition can be written in terms of the S matrix, which is defined by [106]

$$\psi^{(i)}(R \to \infty) \propto \sum_f \left(\frac{e^{-i(k_f R - l_f \pi/2)} \delta_{fi} - e^{i(k_f R - l_f \pi/2)} S_{fi}}{2i} \right). \tag{3.7}$$

S_{fi} is the multichannel scattering matrix.

With this boundary condition in Eq. (3.7) and the solution to Eq. (3.5), we can invert this relation and obtain the S_{fi}. Another way to encapsulate the scattering information is in the T matrix, T_{fi}. This is defined as [104]

$$T_{fi} = i(S_{fi} - \delta_{fi}). \tag{3.8}$$

The S and T matrices have significant meaning in scattering theory [104]. The S matrix is the operator that evolves the quantum state from its incident state ($|\psi_0\rangle$) to its final state including scattering, $\hat{S}|\psi_0\rangle = |\psi_0\rangle + |\psi_{sc}\rangle$, where $|\psi_{sc}\rangle$ is the scattered fraction of the final state. Thus, the S matrix has information about both scattered and unscattered contributions to the final wavefunction. If we compare $|\psi_0\rangle + |\psi_{sc}\rangle$ to the form of the solution given in Eq. (3.3), we find that $|\psi_0\rangle$ is the incident plane wave and $|\psi_{sc}\rangle$ is the spherically symmetric scattered wave. The T matrix, or transfer matrix, is the operator that accounts for just the scattered portion of the final wavefunction: $T|\psi_0\rangle = -i|\psi_{sc}\rangle$.

Physical observables, such as the partial cross section, can be extracted from the T matrix, [104]:

$$\sigma_{fi} = \frac{\pi}{k_i^2}|T_{fi}|^2. \tag{3.9}$$

This quantity describes how much incident flux in state i is scattered into state f. It has units of scattering flux per incident flux per unit area or area. Specifically σ_{fi} is the quantity that describes how likely it is that molecules entering in channel i are converted into channel f by their interaction. If the molecules in channel i are identical, then there is an additional factor of 2 required because of symmetry requirements [106]. Another quantity commonly used to describe collisions is the rate constant $K_{if} = v_i\sigma_f$, where v_i is the incident speed of the colliding particles.

One can rewrite the boundary condition in Eq. (3.7) in terms of real-valued spatial functions. In doing so, we must introduce the solutions to Eq. (3.5) when the $V_{fi} = 0$.

They are proportional to spherical Bessel functions: $\langle R|\psi_f^{(i)}\rangle = \sqrt{\frac{2m_r}{\pi\hbar^2 k_f}} k_f R j_{l_f}(k_f R)$ and $\sqrt{\frac{2m_r}{\pi\hbar^2 k_f}} k_f R n_{l_f}(k_f R)$. Here we have picked the prefactor so that these functions are energy normalized.[2] Spherical Bessel functions have the asymptotic form

$$\begin{aligned} kRj_l(kR \to \infty) &\sim \sin(kR - l\pi/2) \\ kRn_l(kR \to \infty) &\sim \cos(kR - l\pi/2). \end{aligned} \tag{3.10}$$

j_l (n_l) is referred to as the regular (irregular) solution.

Using these solutions to Eq. (3.5), we can write the large R boundary condition in terms of the K matrix. This is

$$\psi^{(i)}(R \to \infty) \propto \sum_f k_f R \left(j_{l_f}(k_f R)\delta_{fi} - n_{l_f}(k_f R) K_{fi} \right). \tag{3.11}$$

It is from this representation that the scattering phase shift (δ_i) emerges. The scattering phase shift is found by using the asymptotic form of the Bessel functions in Eq. (3.10) with trigonometric identities to write the diagonal portion of the wavefunction as

$$\begin{aligned} \psi_i^{(i)} \quad &\propto \cos(\delta_i)\sin(k_i - l\pi/2) + \sin(\delta_i)\cos(k_i - l\pi/2) \\ &\propto \cos(\delta_i)\{\sin(k_i - l\pi/2) + \tan(\delta_i)\cos(k_i - l\pi/2)\} \\ &\propto \sin(k_i - l\pi/2 + \delta_i). \end{aligned} \tag{3.12}$$

It is from the second equation here that we see the diagonal K_{ii} is related to $\tan(\delta_i)$. Ultimately a partial cross section is related to the phase shift $\sigma_{ii} = \frac{4\pi}{k_i^2}\sin^2(\delta_i)$.

There is a possibility of a channel being energetically forbidden at large R. This implies $E_j - E > 0$, which means k_j is purely imaginary, and the asymptotic solutions of Eq. (3.5) are growing and decaying exponentials. To get a physical wavefunction, we demand an exponentially decaying solution in this channel. To do so, we enforce the boundary condition such that

$$\psi_f^{(i)}(R \to \infty) \propto e^{-k_f R}. \tag{3.13}$$

[2] If we denote the wavefunction simply as $\langle R|g_\epsilon\rangle = \sqrt{\frac{2m_r}{\pi\hbar^2 k}} kRj_l(kR)$, where $k = \sqrt{2m_r\epsilon}$. Then the normalization is $\langle g_\epsilon|g_{\epsilon'}\rangle = \delta(\epsilon - \epsilon')$.

This is achieved by taking the appropriate linear combination of mathematical solutions such that the wavefunction at large R decays in the f^{th} channel.

3.2 Field Dressing

In the previous chapter, we explored the effects of external fields on individual molecules. Now it is time to incorporate the effects of external fields into the collision of polar molecules. The effect of an external field is felt in two places in Eq. (3.2), first in H_{int} and second in $\underline{V}$. We will discuss how the field enters into H_{int} and $\underline{V}$, and how they are influenced by external fields. First, we discuss the notation that we use to explain field dressing.

To illustrate ket notation and its utility, we show its equivalent in matrix notation. A state vector, $|\breve{\cup}\rangle$, can be represented in an appropriate basis, say α. This representation could represent anything from spatial coordinates to spin states. Writing the state in the α representation we find: $\sum_a |\alpha_a\rangle\langle\alpha_a|\breve{\cup}\rangle$, where $\langle\alpha_a|\breve{\cup}\rangle$ is the projection of $|\breve{\cup}\rangle$ onto the a^{th} component of the α basis. If there is another equivalent representation, say β, we could write $|\breve{\cup}\rangle = \sum_b |\beta_b\rangle\langle\beta_b|\breve{\cup}\rangle$. An important concept is the relationship between the two representations. Since α and β are equivalent, one must be able to transform a state initially given in the α representation into the β representation. The relationship between the two representations is a unitary transformation. Changing representation α to β is

$$|\breve{\cup}\rangle = \sum_{ba} |\beta_b\rangle\langle\beta_b|\alpha_a\rangle\langle\alpha_a|\breve{\cup}\rangle. \tag{3.14}$$

Here we identify $\sum_{ba} |\beta_b\rangle\langle\beta_b|\alpha_a\rangle\langle\alpha_a|$ as the unitary transformation operator, labeled $\underline{U}^\dagger$. An individual element of this matrix is $U^\dagger_{ba} = \langle\beta_b|\alpha_a\rangle$, which describes how the b^{th} component of β basis projects onto the a^{th} component of the α basis.

In Eq. (3.2), we have H_{int}; in Eq. (3.5), we have $E_f\delta_{fi}$. Because we have used a basis which diagonalized H_{int}, we say we are using the field-dressed basis. This is

necessary numerically because if H_{int} were not diagonal, then it could have nonzero channel couplings at large R that prevents the numerical convergence of a solution. But more importantly, the basis that diagonalizes H_{int} is the set of physical states of the two molecules when they are infinitely separated.

To illustrate how to do field dressing, we need to know the form of H_{int}. Using the explicit $|12lm\rangle$ basis, H_{int} can be written as: $\underline{H}_1 \otimes \underline{1}_2 \otimes \underline{1}_{lm_l} + \underline{1}_1 \otimes \underline{H}_2 \otimes \underline{1}_{lm_l}$. Here H_1 and H_2 contain *all* of the Hamiltonians describing the molecular degrees of freedom. This means these Hamiltonians include the molecules' Stark and Zeeman interactions, as well as all other necessary Hamiltonians such as rotation and vibration. Thus using a basis that diagonalizes H_{int} implies that the molecular states composing the channels, $|1\rangle$ and $|2\rangle$, diagonalize their respective Hamiltonians, H_1 and H_2.

We focus on one of the molecular Hamiltonians, H_1, to further explain field dressing. As stated above, field dressing requires using the states that diagonalize the molecular Hamiltonian to compose the scattering basis. For example, if we consider a Hund's case (b) polar molecule, such as RbCs, then H_1 could include the Stark Hamiltonian and the rotation Hamiltonian. Then the undressed field basis would then be the rigid rotor basis, and with a nonzero electric field, the dressed basis would be the eigenstates of H_1. These eigenstates are appropriate linear combinations of rotational states. In general, the undressed basis is the zero-field basis.

To illustrate the effect of field dressing on the molecular interaction, we need to explicitly consider the dressed ($|d\rangle$) and undressed ($|u\rangle$) molecular state bases. We can write the operator H_1 in the undressed basis:

$$H_1 \quad = \sum_{uu'} |u\rangle\langle u|H_1|u'\rangle\langle u'|. \tag{3.15}$$

By diagonalizing the H_1 operator, we obtain the eigenstates, or the find the field-dressed basis, $|d\rangle$, i.e.,

$$H_1|d\rangle = \lambda_d|d\rangle. \tag{3.16}$$

The eigenvectors form the columns of a matrix $\underline{U}$, that can be used to transform between dressed and undressed basis sets.

To give a concrete molecular example, consider the two e and f states of OH without hyperfine structure, where $J = M_J = \bar{\Omega} = 3/2$. The e and f states will be our undressed basis, where $|u_1\rangle = |JM_F\bar{\Omega}e\rangle$ and $|u_2\rangle = |JM_F\bar{\Omega}f\rangle$. We have already composed the Stark Hamiltonian in the undressed basis in Section (2.1.2). The Stark Hamiltonian and the energy splitting between the e and f states, Δ, is:

$$H_1 = \begin{pmatrix} 0 & q \\ q & \Delta \end{pmatrix}, \tag{3.17}$$

where $q = \mu\mathcal{E}M\Omega/J(J+1)$, as given in Eq. (2.23). This equation can be diagonalized analytically, yielding the energy eigenvalues: $\lambda_1 = \frac{1}{2}\left(\Delta - \sqrt{\Delta^2 + 4q^2}\right)$ and $\lambda_2 = \frac{1}{2}\left(\Delta + \sqrt{\Delta^2 + 4q^2}\right)$. The eigenstates or field-dressed states are $|d_1\rangle = c_1^{(1)}|u_1\rangle + c_2^{(1)}|u_2\rangle$ and $|d_2\rangle = c_1^{(2)}|u_1\rangle + c_2^{(2)}|u_2\rangle$. For this example, these field-dependent coefficients are analytic and are $c_1^{(1)} = c_2^{(2)} = \sqrt{\frac{1}{2}\left(1 + \frac{\Delta}{\sqrt{\Delta^2+4q^2}}\right)}$ and $c_1^{(2)} = -c_2^{(1)} = \sqrt{\frac{1}{2}\left(1 - \frac{\Delta}{\sqrt{\Delta^2+4q^2}}\right)}$. However in general, the $c_n^{(m)}$s are numerically determined.

A molecular operator written in the undressed basis can be transformed into the dressed basis by using a linear transformation:

$$\begin{aligned} \underline{\lambda} \quad &= \underline{U}^\dagger \underline{H}_1 \underline{U} \\ &= \sum_{dud'u'} |d\rangle\langle d|u\rangle\langle u|H_1|u'\rangle\langle u'|d'\rangle\langle d'| \\ &= \sum_d \lambda_d |d\rangle\langle d|. \end{aligned} \tag{3.18}$$

Between the second and third line, we have used Eq. (3.16) and $\langle d|d'\rangle = \delta_{dd'}$.

In the OH example, we can transform the operator H_1 from the undressed basis to the dressed basis by constructing $\underline{U} = \begin{pmatrix} c_1^{(1)} & c_1^{(2)} \\ c_2^{(1)} & c_2^{(2)} \end{pmatrix} = \begin{pmatrix} \langle u_1|d_1\rangle & \langle u_1|d_2\rangle \\ \langle u_2|d_1\rangle & \langle u_2|d_2\rangle \end{pmatrix}$. Then H_1 in the dressed basis is

$$\underline{\lambda} \quad = \underline{U}^\dagger \underline{H}_1 \underline{U} \tag{3.19}$$

$$= \begin{pmatrix} c_1^{(1)} & c_2^{(1)} \\ c_1^{(2)} & c_2^{(2)} \end{pmatrix} \begin{pmatrix} 0 & q \\ q & \Delta \end{pmatrix} \begin{pmatrix} c_1^{(1)} & c_1^{(2)} \\ c_2^{(1)} & c_2^{(2)} \end{pmatrix} \tag{3.20}$$

$$= \begin{pmatrix} \frac{1}{2}(\Delta - \sqrt{\Delta^2 + 4q^2}) & 0 \\ 0 & \frac{1}{2}(\Delta + \sqrt{\Delta^2 + 4q^2}) \end{pmatrix}. \tag{3.21}$$

There is a lot of algebra to get between the second and third lines but it does work, and it had better, because we picked the dressed basis such that H_1 was diagonal.

Now that we have diagonalized the molecular Hamiltonians, we can construct the field-dressed scattering basis, i.e., for a given channel $|12lm_l\rangle$, $|1\rangle$ and $|2\rangle$ are the energy eigenstates of the field. We can see where the scattering thresholds originate from when acting on H_{int}. The result is

$$\begin{aligned} \langle 12lm_l|H_{int}|1'2'l'm_l'\rangle &= \langle 12lm_l|\underline{H}_1 \otimes \underline{1}_2 \otimes \underline{1}_{lm_l} + 1_1 \otimes \underline{H}_2 \otimes \underline{1}_{lm_l}|1'2'l'm_l'\rangle \\ &= (\lambda_1 + \lambda_2)\delta_{11'}\delta_{22'}\delta_{ll'}\delta_{m_l m_l'} \\ &= \langle \phi_f|\underline{H}_{int}|\phi_i\rangle = E_f\delta_{fi}. \end{aligned} \tag{3.22}$$

The last line uses the notation in Eq. (3.5) and corresponds f (i) to the unprimed (primed) states.

Field dressing the molecular interaction accounts for the effect of the field on the molecules, and consequently using the field-dressed molecular interaction accounts for the field's influence on the interaction. To compute the interaction, we first construct the molecular interaction in the undressed basis (we only need to do this once), and then for a particular value of the field, we need to construct the transformation between the dressed and undressed basis. Then the field-dressed molecular interaction is

$$\langle 12lm_l|V(R)|1'2'l'm_l'\rangle = \tag{3.23}$$

$$\sum_{u_1u_2u_1'u_2'} \langle 12lm_l|u_1u_2lm_l\rangle \times\langle u_1u_2lm_l|V(R)|u_{1'}u_{2'}l'm_l'\rangle \times\langle u_{1'}u_{2'}l'm_l'|1'2'l'm_l'\rangle. \tag{3.24}$$

Here we use $|u_i\rangle$ to denote the undressed basis of the i^{th} molecule. This expression shows us that the external field can change the way in which the colliding molecules interact to rearrange the couplings. The field dressing can also be written in matrices. The transformation matrix is $\underline{U}_1^\dagger \otimes \underline{U}_2^\dagger \otimes \underline{1}_{lm_l}$. An individual element of this matrix is $\langle 12lm_l|u_1u_2l'm_l'\rangle$, where an element is $\langle 1|u_1\rangle\langle 2|u_2\rangle\delta_{ll'}\delta_{m_lm_l'}$, which is the product of coefficients from the individual molecular field dressing matrices: $\underline{U}_1^\dagger$ and $\underline{U}_2^\dagger$.

3.3 Symmetrized Wavefunction

If the molecules are identical particles, then their wavefunction must be properly symmetrized. For bosons (fermions) the wavefunction must be symmetric (antisymmetric) upon particle exchange. There are two operations to ensure this symmetry: one must both swap internal coordinates of the molecules and spatially invert the coordinate system. This implies that the angular and molecular state components, $Y_{l_fm_{l_f}}(\theta,\phi)\chi_{n_f}$, carry the symmetry of the wavefunction. Under spatial inversion, $\hat{I}$, the spherical harmonics have the property

$$\hat{I}Y_{lm}(\theta,\phi) \rightarrow Y_{lm}(\pi-\theta,\phi+\pi) = (-1)^l Y_{lm}(\theta,\phi). \tag{3.25}$$

To complete the symmetrization, we construct a symmetric basis under particle exchange. The symmetrized basis is

$$|12\rangle_s = \frac{|12\rangle + s|21\rangle}{\sqrt{2(1+\delta_{12})}}. \tag{3.26}$$

Here s denotes the exchange symmetry of the molecular basis set and δ_{12} implies a delta function for all molecular quantum numbers. For bosons (fermions), we need $s(-1)^l$ to be positive (negative). Therefore if we have a pair of indistinguishable bosons (fermions), s must be 1, then we must restrict l to even (odd) values. For a complete discussion of symmetry properties in cold collisions see Ref. [106].

3.4 Dipole-Dipole Interaction

The molecular interaction has many contributions. However, for the purposes of our studies, we focus solely on the dipole-dipole interaction. The justification for this is that all other long range forces are much smaller, such as the quadrupole-quadrupole and dispersion interactions [91]. With regards to the short-range interaction, there are generally no accurate potential energy surfaces (PESs). Even without PESs, the collisions of ultracold polar molecules are intriguing because at near zero collision energies, the dipolar interaction strongly influences the molecular scattering. For example, in the scattering of weak-field seekers, it has been found that the scattering is nearly purely long range in nature [87]; this prevents the molecules from reaching short range. However, for strong-field seekers, there is no way to avoid short-range interactions. This makes it necessary to approach scattering and its result with the intention of eventually adding the PES or a parameterization accounting for short-range molecular interaction. Even without short-range interaction, much can be learned from studying the dipolar interaction. The primary result will be an understanding of the long-range scattering, which can lead the way for a clear comprehension of the full molecular interaction. We will now discuss the general form of the dipole-dipole interaction.

The dipole-dipole interaction is long range and anisotropic. The interaction in vector form is [96]

$$H_{\mu\mu} = -\frac{3(\hat{\mathbf{R}}\cdot\hat{\mu}_1)(\hat{\mathbf{R}}\cdot\hat{\mu}_2) - \hat{\mu}_1\cdot\hat{\mu}_2}{R^3}, \tag{3.27}$$

where $\hat{\mu}_i$ is the dipole moment of molecule i, R is the intermolecular separation, and $\hat{\mathbf{R}}$ is the unit vector defining the intermolecular axis. This interaction is conveniently rewritten in terms of tensorial operators as [106]:

$$H_{\mu\mu} = -\frac{\sqrt{6}}{R^3}\sum_q (-1)^q C^2_{-q}\cdot(\mu_1\otimes\mu_2)^2_q. \tag{3.28}$$

Here $C^2_{-q}(\theta,\phi)$ is a reduced spherical harmonic that acts on the relative angular coordinate of the molecules, while $(\mu_1\otimes\mu_2)^2_q$ is the second rank tensor formed from two rank

one operators found in the Stark Hamiltonian. For this reason, matrix elements of the interaction are given conveniently in terms of the matrix elements in Eq. (2.5).

The physical significance of this fact originates from the dipole-dipole interaction describing how a molecule's dipole field influences another molecule's dipole when they scatter. Thus to understand the form of the interaction, we need to understand how an electric field influences a polar molecule, which we have done with the Stark effect. Therefore the matrix elements of the dipolar interaction are:

$$\begin{aligned}\langle 12lm_l|H_{\mu\mu}|1'2'l'm_l'\rangle &= (-1)^{-m_l+m_l'+1}\left(\frac{\mu^2\sqrt{6}}{R^3}\right)\\ \times\langle lm_l|C^2_{(m_l-m_l')}|l'm_l'\rangle&\langle\alpha_1F_1M_{F_1}|D^{1\star}_{q_10}|\alpha_1'F_1'M_{F_1}'\rangle\\ &\times\langle\alpha_2F_2M_{F_2}|D^{1\star}_{q_20}|\alpha_2'F_2'M_{F_2}'\rangle\\ \times\begin{pmatrix} 1 & 1 & 2\\ M_{F_1}-M_{F_1}' & M_{F_2}-M_{F_2}' & m_l-m_l'\end{pmatrix},\end{aligned} \tag{3.29}$$

where

$$\begin{aligned}\langle lm_l|C^2_{(m_l-m_l')}|l'm_l'\rangle &= (-1)^{m_l}[l,l']\begin{pmatrix} l & 2 & l'\\ 0 & 0 & 0\end{pmatrix}\\ &\times\begin{pmatrix} l & 2 & l'\\ -m_l & m_l-m_l' & m_l'\end{pmatrix}.\end{aligned} \tag{3.30}$$

Here we have used $q_1 = M_{F_1} - M_{F_1}'$ and $q_2 = M_{F_2} - M_{F_2}'$. Equation (3.29) shows that once the Stark Hamiltonian has been constructed for a particular molecule by obtaining the matrix elements $\langle\alpha FM_F|D^{1\star}_{q0}|\alpha'F'M_F'\rangle$, then the Hamiltonian describing the dipolar interaction can be achieved with little extra effort. This general form applies to all rigid rotor molecules.

Equations (3.27) and (3.28) are the general form of the dipole-dipole interaction. They can be electric dipoles or magnetic dipoles. For polar molecules the interaction of electric dipoles is much larger than magnetic dipoles. This can be seen by comparing the size of the dipoles that appear in Eq. (3.27). For polar molecules, the dipole

originates from a charge distribution, and this can lead to electric dipoles of order 1 (a.u.). For magnetic dipoles, whose origin is the intrinsic spin of the electron, have a magnetic dipole on the order of $\alpha \sim 1/137$ (a.u.), the fine structure constant. Since the interaction goes as μ^2, one can see that the electric dipole-dipole interaction can be much larger.

3.5 The Born Approximation

The behavior of the dipolar interaction is distinct from previously observed non-polar collisions in ultracold gases for two reasons: (1) it is anisotropic and (2) it has distinct threshold behavior. There is a large body of work on the threshold behavior of collisions, or scattering behavior, as the energy goes to zero. For a review of the threshold work see Ref. [107] and references therein. Generally, threshold laws depend on both the partial wave and the intermolecular potential, $\sim 1/R^s$. The scattering phase shift can be written as

$$\delta \propto \alpha k^{2l+1} + \beta k^{s-2}. \tag{3.31}$$

The coefficients α and β depend on the details of the potential. For the dipolar interaction where $s = 3$, the second term dominates for $l > 0$ where $\delta \sim k$. This shows us that the potential has a significant effect on the scattering properties as the collision energy approaches zero.

To first explore the threshold behavior, we use the Born approximation [104, 105]. We consider the dipolar interaction to be small. Then we can expand the wavefunction in terms of spherical Bessel functions that comprise the unperturbed incident plane wave. We can then use the Born approximation to study the threshold behavior. Here we follow the discussion laid out by Refs. [88, 105].

To first order, the Born approximation gives the T matrix as

$$\langle f|T|i\rangle \propto \langle f|V|i\rangle. \tag{3.32}$$

Here $\langle f|T|i\rangle$ is a more explicit way of writing T_{fi}, which relates the molecular interaction to changes in the molecular state from $|i\rangle$ to the final state $|f\rangle$. Using the Bessel functions and the potential in Eq. (3.28), we find the Born approximation gives us the following approximation to the T matrix [105]

$$\langle f|T|i\rangle = 2\left(\frac{2m_r}{\hbar^2}\right)\sqrt{k_i k_f}\int_0^\infty R^2 dR j_{l_f}(k_f R)\frac{C_3(fi)}{R^3}j_{l_i}(k_i R). \tag{3.33}$$

Here we have used $C_3(fi)$ to represent the coupling between the channels i and f, which is given by Eq. (3.29).

There are two cases we wish to discuss: (1) the elastic case ($k_i = k_f$) and (2) the inelastic, exothermic case ($k_i < k_f$) as $k_i \to 0$. The elastic case be solved for $l_i + l_f > 0$ and gives the result

$$\langle f|T|i\rangle = \frac{4m_r C_3(fi)}{\hbar^2}k_i\left(\frac{\pi\Gamma\left(\frac{l_i+l_f}{2}\right)}{8\Gamma\left(\frac{-l_i+l_f+3}{2}\right)\Gamma\left(\frac{l_i+l_f+4}{2}\right)\Gamma\left(\frac{l_i-l_f+3}{2}\right)}\right), \tag{3.34}$$

where Γ is a gamma function. The important feature of this result is $T_{fi} \sim k_i$, which means the cross section for any incident partial wave does *not* vanish in the zero-energy limit.

The inelastic case can also be solved for $l_i + l_f > 0$.

$$\langle f|T|i\rangle = \frac{4m_r C_3(fi)}{\hbar^2}\left(\frac{k_i^{l_i+1/2}\Gamma\left(\frac{l_i+l_f}{2}\right)}{4k_f^{l_f-1/2}\Gamma\left(\frac{-l_i+l_f+3}{2}\right)\Gamma\left(l_i+3/2\right)}\right) \times F\left(\frac{l_i+l_f}{2}, \frac{l_i-l_f-1}{2}, 3/2; \left(\frac{k_i}{k_f}\right)^2\right), \tag{3.35}$$

where F is a hypergeometric function. The importance of this result is if we have $k_f >> k_i$, which is the case for ultracold exothermic collisions, then we find the leading order term of hypergeometric function is a constant. Thus Eq. (3.35) gives us $T_{fi} \sim k_i^{l_i+1/2}$. This leads to $\sigma_{fi} \sim k_i^{2l_i-1} \sim E_i^{l_i-1/2}$. This result shows us that for an incident channel with s-wave character, the cross section diverges as the collision energy goes to zero.

3.6 Adiabatic Representation and the Born Approximation

The ordinary Born approximation is useful for getting a feel for the threshold behavior, but the form given above does not help interpret our results when the dipolar interaction is strong. To improve upon the Born approximation for our applications, we use the adiabatic representation [91, 105]. This representation allows us to more accurately represent the wavefunctions and channel coupling for the molecular systems. The adiabatic representation assumes that R is a "slow" coordinate. At every R, we diagonalize the Hamiltonian in all remaining degrees of freedom. Since it is not rigorously true that R varies infinitely slowly, the residual nonadiabatic couplings can be accounted for in the kinetic energy operator. In a more formal treatment, we diagonalize

$$\underline{W} = \left(\frac{\hbar^2 l(l+1)}{2m_r R^2} \underline{1} + \underline{V}(R) + \underline{H}_{int} \right), \tag{3.36}$$

where the terms are, respectively, the centrifugal barrier, potential matrix including dipole-dipole interaction, and the molecular Hamiltonian in the diabatic representation. Diagonalizing the matrix in Eq. (3.36), we get $\underline{W}|\alpha(R)\rangle = U_\alpha(R)|\alpha(R)\rangle$, where $U_\alpha(R)$ are the eigenvalues and $|\alpha(R)\rangle$ are the eigenvectors. With the eigenvectors we are able to form a linear transformation $\underline{X(R)}$ that transforms between the diabatic and adiabatic representations, i.e., $\underline{X}^T \underline{W}(R) \underline{X} = \underline{U}(R)$. The eigenvalues and eigenvectors have radial dependence but for notational simplicity (R) will be suppressed hereafter.

To distinguish between adiabatic and diabatic representations, we use Greek letters $(\alpha, \beta, ...)$ to denote the adiabatic channels and Roman letters (i,j,...) to denote diabatic channels. When considering specific inelastic processes in the diabatic basis, we denote initial and final channels as i and f and the adiabatic channels as ι and φ. In the limit $R \to \infty$, the two sets of channels coincide. The transformation between the representations is R dependent, implying that the channel couplings shift from the potential to the kinetic energy operator. Using the adiabatic representation changes

Eq. (3.5) to

$$\left(\underline{X}^T \frac{-\hbar^2}{2m_r}\frac{d^2}{dR^2}\underline{X} + \underline{U}\right)\vec{\xi}(R) =$$
$$\left(\frac{-\hbar^2}{2m_r}\left(\frac{d^2}{dR^2} + 2\underline{P}\frac{d}{dR} + \underline{Q}\right) + \underline{U}\right)\vec{\xi}(R) = E\vec{\xi}(R). \tag{3.37}$$

Here $\vec{\xi} = \underline{X}^T\vec{\psi}$, with $\psi^{(i)}$ written in vector notation.

To get the channel couplings in the adiabatic picture, we need matrix elements of the derivative operators, defined as $P_{\alpha\beta} = \langle\alpha|\frac{d}{dR}|\beta\rangle$ and $Q_{\alpha\beta} = \langle\alpha|\frac{d^2}{dR^2}|\beta\rangle$. We evaluate the $P_{\alpha\beta}$ matrix, the dominant off-diagonal channel coupling, using the Hellmann-Feynman theorem [105]

$$P_{\alpha\beta} = \frac{\sum_{kl} X^T_{\alpha k}\nabla V_{kl} X_{l\beta}}{U_\alpha - U_\beta}. \tag{3.38}$$

In general, the contribution of Q is much smaller than P, so consequently we ignore Q for this analysis.

Scattering amplitudes are then easily estimated in the adiabatic-distorted-wave Born approximation (ADWBA). Namely, we construct incident and final radial wave functions $\phi_{\iota,\varphi}$ that propagate according to the adiabatic potentials $U_{\iota\varphi}$. In terms of these adiabatic wavefunctions, the scattering T-matrix is given by an overlap integral analogous to Eq. (3.33) [105]

$$T_{\iota\varphi} = \frac{\pi\hbar^2}{m_r}\langle\phi_\iota|\frac{\overleftarrow{d/dR}\underline{P} + \underline{P}\overrightarrow{d/dR}}{\sqrt{2}}|\phi_\varphi\rangle. \tag{3.39}$$

Here $\overleftarrow{d/dR}$ ($\overrightarrow{d/dR}$) is the radial derivative operator acting to the left (right). The cross section for identical bosons is $\sigma_{\iota\varphi} = \frac{2\pi}{k_\iota^2}|T_{\iota\varphi}|^2$. From here we are able to numerically calculate a rate constant for inelastic loss $K_2^{inel} = v_\iota\sigma_{\iota\varphi}$, where v_ι is the asymptotic velocity given by $\sqrt{2U_\iota(R\to\infty)/m_r}$.

3.7 Numerical Techniques

Modeling molecular collisions is a large numerical undertaking. A typical OH scattering problem in a field involves several hundred channels to be simultaneously

solved. To do these calculations, we have used the Johnson log-derivative propagator [108], which numerically propagates the Y matrix in R. The Y matrix is $\underline{Y} = \underline{\psi'\psi^{-1}}$, where $\psi' = \frac{d}{dR}(\psi)$. We also used the R-matrix method with finite element basis numerical techniques to produce wavefunctions [106].

Once we numerically calculated the Y matrix, we could apply boundary conditions and solve for the K matrix. The wavefunction is $\underline{\psi} \propto \underline{f} - \underline{g}\underline{K}$, where $\underline{f}$ ($\underline{g}$) is diagonal matrix with the regular (irregular) solution as its entries, these functions are the energy-normalized spherical Bessel functions. Since we have numerically solved for the Y matrix, we can solve for the K matrix in terms of $\underline{f}$, $\underline{g}$, and $\underline{Y}$. Thus the K matrix is $\underline{K} = (\underline{Y}\underline{g} - \underline{g}')^{-1}(\underline{Y}\underline{f} - \underline{f}')$. With the K matrix, all physical observables can be determined. For more details on such matters, see Ref. [106].

Chapter 4

Weak-Field Seekers in the Presence of Magnetic and Electric Fields

As the experimental reality of trapping ultracold polar molecules approaches, a clear understanding is needed of how the molecules interact in the trap environment. On the most straightforward level, collisions are essential for cooling the gas by either evaporative or sympathetic cooling methods. A high rate of elastic collisions is desirable, while a low rate of exothermic, state-changing collisions is essential if the cold gas is to survive at all.

One promising strategy for trapping ultracold molecules might be to follow up on successes in trapping cold atoms and to construct electrostatic [56, 109] or magnetostatic [52] traps that can hold molecules in a weak-field-seeking state. Cold collisions of polar molecules in this environment have been analyzed in the past, with the finding that inelastic collision rates were unacceptably high in the presence of the electric field, limiting the possibilities for stable trapping [87]. Reference [87] found that the large inelastic rates were due to the strong dipole-dipole interaction between the molecules. One important feature of the dipole-dipole interaction is its comparatively long range. Even without knowing the details of the short-range molecule-molecule interactions, the dipole forces alone were sufficient to change the internal molecular states. Indeed, a significant finding was that for weak-field seekers, the molecules are prevented from approaching close to one another due to a set of long-range avoided crossings. Therefore, a reasonably accurate description of molecular scattering may be made using the dipolar

forces alone [90].

A complimentary set of theoretical analysis have considered the problem of collisional stability of paramagnetic molecules in a magnetostatic trap. For example, the weak-field-seeking states of molecules are expected to survive collisions with He buffer gas atoms quite well [110, 111]. Collisions of molecules with each other are also expected to preserve their spin orientation fairly well, and hence remain trapped [87]. However, this effect is mitigated in the presence of a magnetic field [85, 112].

So far, no one appears to have considered the influence of *magnetic* fields on cold molecule-molecule collisions where both species have *electric* dipole moments. The effects of magnetic and electric fields were contrasted in Section 2.2, and in this chapter, we approach their use to control collisions; we consider cold OH($^2\Pi_{3/2}$)-OH($^2\Pi_{3/2}$) collisions in an electric or a magnetic field. To the extent that the applied electric field is zero, one might expect that dipole forces average to zero and thus do not contribute to destabilizing the spin orientation. It turns out that this is not quite correct and that dipole-dipole forces still dominate long-range scattering. However, applying a suitably strong magnetic field mitigates this effect significantly. Interestingly, even in this case, the residual second-order dipole interactions are sufficiently strong to restrict scattering to large intermolecular separation.

The main result of the chapter is summarized in Fig. 4.1, which contrasts the influence of electric and magnetic fields. Figure 4.1(a) plots the elastic (solid curves) and inelastic (dashed curves) collision rate constants for OH molecules in their $|FM_F\epsilon\rangle = |22-\rangle$ weak-field-seeking hyperfine state (for details on quantum numbers, see Chapt. 2). As the electric field is increased, the inelastic rate constant grows to alarmingly large values, making the gas collisionally unstable, as was shown in Ref. [87]. Figure 4.1(b) shows the analogous rate constants in a magnetic field (in both cases the field is assumed to lie along the positive z axis of the laboratory reference frame). In this case, the magnetic field has the effect of suppressing collisions all the way down to a

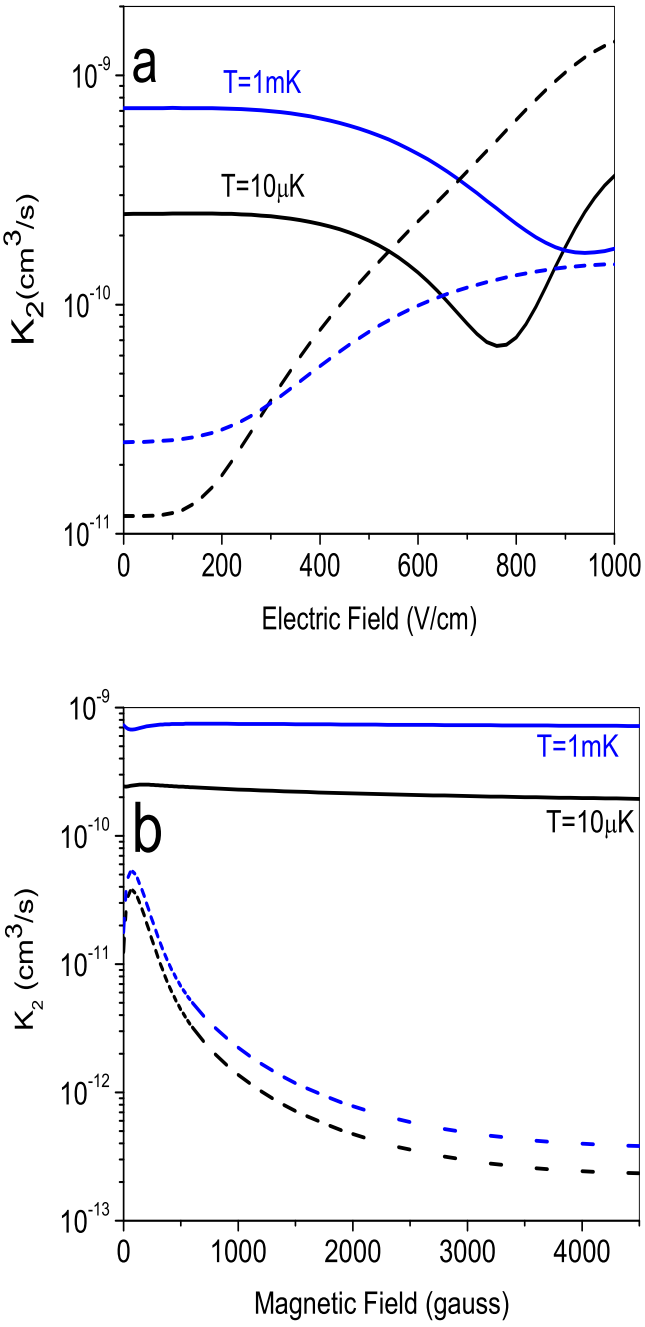

Figure 4.1: Thermally averaged rate constants for collisions of weak-field-seeking states of OH as a function of applied electric field (a) and magnetic field (b). In both cases, solid lines denote elastic scattering rates, while dashed lines denote inelastic scattering rates. Two temperatures are considered. Applying an electric fields drives the inelastic collisions rates up, while an applied magnetic field drives inelastic collision rates down.

rate constant of 2×10^{-13} cm^3/sec at fields of $B = 3000$ Gauss. These results are fairly robust against raising the temperature to the merely cold (not ultracold) temperatures, $\sim 1mK$, attainable in buffer-gas loading or Stark slowing experiments. This is good news for experiments, it implies that cooling strategies that rely on collisions may be feasible, provided a suitably large bias magnetic field is applied.

Our main goal here is to analyze the suppression of rates in a magnetic field. We present an analysis of the system in a magnetic field using a reduced channel model that encapsulates the essential collision physics. Finally, the model is qualitatively understood using the adiabatic representation.

4.1 Inelastic Rates of OH-OH Collisions in External Fields

We now study the consequences of the dipolar interaction, Eq. (3.29), on scattering. Scattering calculations are done using the log-derivative propagator method [108]. To ensure convergence at all collision energies and applied fields, it is necessary to include partial waves up to $l = 6$ and to carry the propagation out to an intermolecular distance of $R = 10^4(a.u.)$ before matching to long-range wave functions. Cross sections and rate constants are computed in the standard way for anisotropic potentials [110].

We remind the reader that throughout this chapter we consider collisions of molecules initially in their $|FM_F\epsilon\rangle = |22-\rangle$ states, which are weak-field seeking for both electric and magnetic fields. Thus for a scattering process incident on an s- partial wave, the incident channel will be written $|i\rangle = |F_1 M_{F_1}\epsilon_1\rangle|F_2 M_{F_2}\epsilon_2\rangle|lm_l\rangle = |22,-\rangle|22,-\rangle|00\rangle$.

In this section, we will make frequent reference to "energy gap suppression" of collision rates. This notion arises from a perturbative view of inelastic collisions, in which case the transition probability amplitude is proportional to the overlap integral

$$\int dR \psi_i(R) V_{if}(R) \psi_f(R) \tag{4.1}$$

where $\psi_{i,f}$ denotes the incident and final channel radial wave functions and V_{if} is the

coupling matrix element between them. In our case, ψ_i will have a long de Broglie wavelength corresponding to its essentially zero collision energy. The de Broglie wavelength of ψ_f will instead grow smaller as the energy gap $E_i - E_f$ between incident and final thresholds grows. Thus the integral in Eq. (4.1), and correspondingly the collision rates, will diminish. For this reason, the collisions we consider tend to favor changing the hyperfine states of the molecules over changing the parity states, since the hyperfine splitting of OH is smaller than the Λ-doubling.

4.1.1 Electric Field Case

To calculate scattering in the presence of an electric field, we only need to include partial waves $l = 0, 2$ for numerical accuracy of the inelastic rate constant, K_2^{inel}, for the field range that we consider, $E \leq 1000(V/cm)$, and at a collision energy of 10^{-5} K. Here we are only interested in the trend and identification of the loss mechanism. To numerically converge the inelastic rates at higher field values, where the induced dipoles are large, naturally requires more partial waves.

Figure 4.2 (a) shows the total (black) and partial (color) inelastic rate constant K_2^{inel} as a function of the electric field [compare to Fig. 4.1 (a)]. Even in zero field, where the dipolar forces nominally average out, the rate constant is large, comparable to the elastic rate constant. This fact attests to the strength of dipolar forces in OH, even in second order.

The green line in Fig. 4.2(a) represents losses to the dominant zero-field loss channel $|10-\rangle|22-\rangle|22\rangle$. The blue curve in Fig. 4.2 (a) represents instead the dominant loss process at higher electric field values in channel $|21-\rangle|22-\rangle|21\rangle$. Whereas the former rate remains relatively insensitive to field, the latter rises dramatically.

This behavior arises from two competing tendencies in an electric field. The first is the increasing mixing of different parity states as the field is turned on, leading to an increasing strength of the direct dipole-dipole coupling that affects both exit channels.

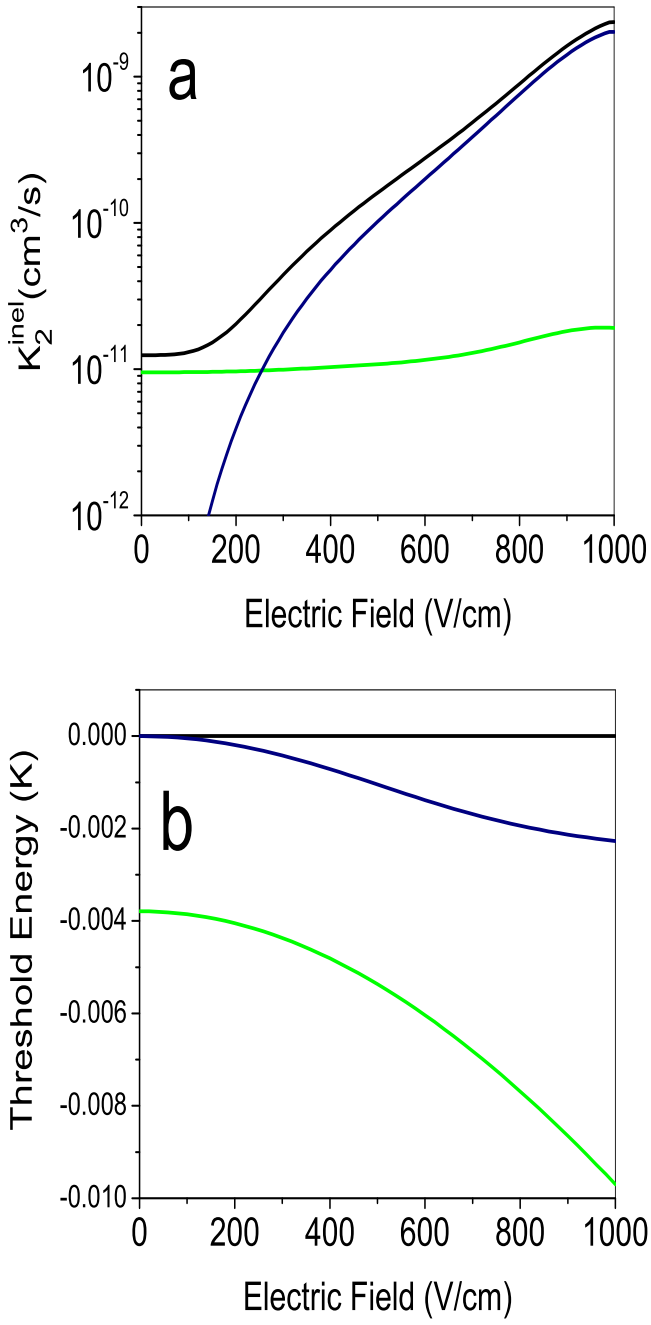

Figure 4.2: (a) Total (black) and selected partial (color) inelastic rates for OH-OH collisions as a function of electric field. The green curve is the dominant zero field inelastic loss process to channel $|10-\rangle|22-\rangle|22\rangle$ (green). In the presence of the field, a different channel, $|21-\rangle|22-\rangle|21\rangle$, becomes dominant (blue). (b) The thresholds for these exit channels, relative to the incident threshold.

This additional coupling would, in general, cause inelastic rates to rise. It is, however, offset by the competing tendency for inelastic rates to become less likely when the change in relative kinetic energy of the collision partners is larger. Figure 4.2(b) shows the threshold energies for the two exit channels in Fig. 4.2(a), versus field, with zero representing the energy of the incident threshold. Here it is evident that loss to the channel $|22-\rangle|10-\rangle|22\rangle$ (green line) is accompanied by a large gain in kinetic energy, whereas loss to channel $|21-\rangle|22-\rangle|21\rangle$ (blue line) gains comparatively little kinetic energy, and thus the later channel more strongly affected by the increased coupling generated by the field.

4.1.2 Magnetic Field Case

To gain insight into the suppression of the inelastic rates in a magnetic field [Fig. 4.3 (a)], calculations were at a representative collision energy $E = 10^{-5}K$. To converge the calculations in high field (B$\geq$ 1500 Gauss) required partial waves $l = 0, 2, 4, 6$. We have only considered collisions with incident partial wave $l = 0$, since higher partial wave contributions, while they exist, only contribute to rates at the fraction of a percent level.

Because the electric field remains zero, parity is still a rigorously good quantum number. Therefore states of the same parity are not directly coupled. Nevertheless, the dominant loss channels in a magnetic field share the parity of the incident channel wave function, $|i\rangle = |22, -\rangle|22, -\rangle|00\rangle$. Figure 4.3 (a) illustrates this by showing the total (black) and partial (color) inelastic rates as a function of the magnetic field. The loss rates shown correspond to the exit channels $|f\rangle = |10-\rangle|22-\rangle|22\rangle$(green), $|11-\rangle|22-\rangle|41\rangle$(blue), and $|10-\rangle|10-\rangle|44\rangle$(red).

Since direct coupling to the final channels is forbidden to the dipolar interaction, all coupling must occur through some intermediate channel $|int\rangle$. Moreover, owing to the parity selection rules in the matrix element [Eq. (3.29)], this intermediate channel must have parity quantum numbers $\epsilon_1 = \epsilon_2 = +$. Since this coupling is second order,

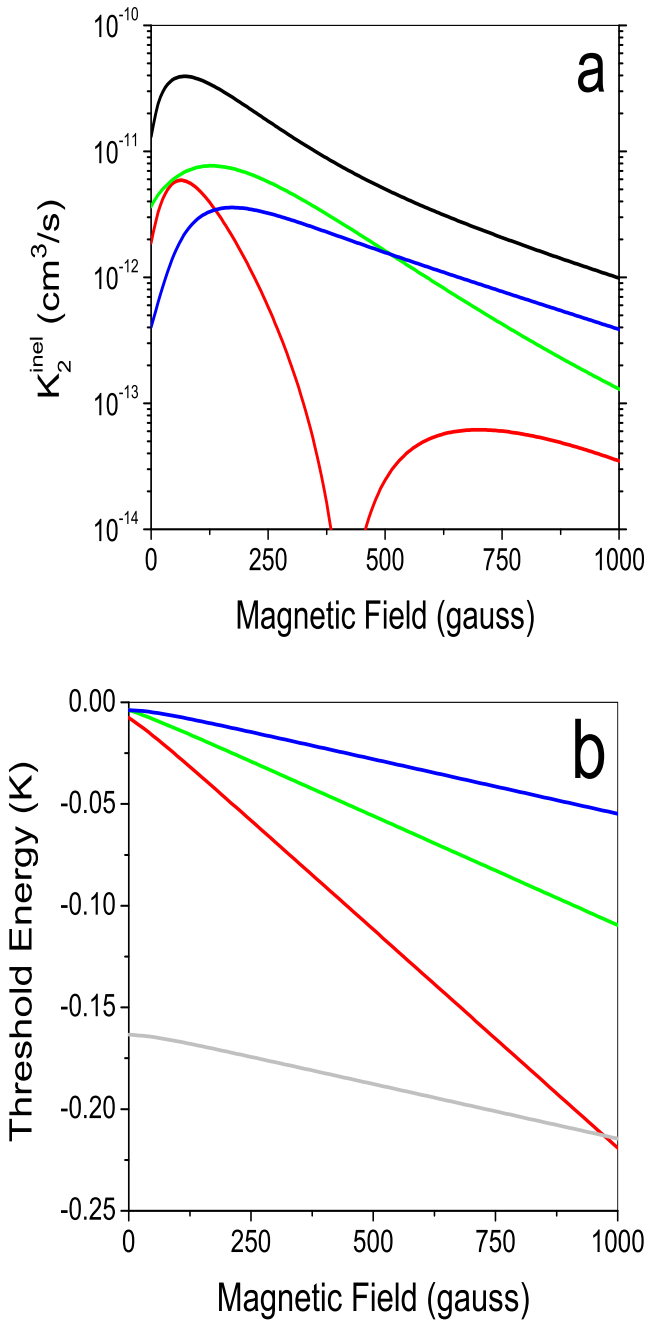

Figure 4.3: (a) The total (black) and partial (color) inelastic rates for OH-OH collisions as a function of magnetic field. The colors are explained in the text. (b) The corresponding thresholds, referred to the incident channel's threshold ($E_i = 0$). The lowest curve is one possible intermediate channel.

the dominant exit channels can consist of both d-wave ($l_f = 2$) and g-wave ($l_f = 4$) contributions, in contrast to the electric field case.

The primary feature of the inelastic rates in Fig. 4.3 (a) is that they decrease significantly at large field. This decline is the main reason for optimism regarding evaporative cooling strategies in OH; an applied bias field of 3000 Gauss can reduce the inelastic rate constant to below 2×10^{-13} cm^3/sec (see Fig. 4.1). The cause of this decrease can be traced directly to the relative separation of the incident and final channel thresholds, along with the indirect nature of the coupling.

To see this, we reduce the model to its essential ingredients: (1) a strong dipole-dipole interaction, (2) the relative shift of the thresholds as the magnetic field is tuned, (3) an extremely exothermic intermediate channel, and (4) the centrifugal barrier in the final and intermediate channels. The Hamiltonian for a reduced model is $H_{Model} = T_0 + V_{Model}$, where T_0 is the kinetic energy operator and V_{Model} in matrix form is

$$V_{Model} = \begin{pmatrix} E_i & 0 & a/R^3 \\ 0 & E_f + c_f/R^2 & b/R^3 \\ a/R^3 & b/R^3 & E_{int} + c_{int}/R^2 \end{pmatrix}. \tag{4.2}$$

Here c_j is a centrifugal repulsion with $c_j = \hbar^2 l_j(l_j+1)/2m_r$, a and b are dipole-dipole coupling strengths, and E_j is the threshold energies for the j^{th} channel, which mimic the essential feature of the Zeeman effect in this system. The channels $\{i, f, int\}$ have quantum numbers $(\epsilon_1\epsilon_2)^i = (\epsilon_1\epsilon_2)^f = (--)$ and $(\epsilon_1\epsilon_2)^{int} = (++)$. The incident channel has a partial wave $l_i = 0$, while dipole-coupling selection rules allow $l_{int} = 2$ and $l_f = 2$ or $l_f = 4$.

The model Hamiltonian [Eq. (4.2] explicitly excludes direct coupling between incident and final channels, whereas coupling is mediated through the *int* channel. Parameters characteristic of the physical problem are $a = 0.12$ (a.u.), $b = 0.10$ (a.u.), $E_i = 0$, $E_f = -0.003 \rightarrow -0.1(K)$, and $E_{int} = -0.17(K)$, $l_i = 0$, $l_f = 2$ or $l_f = 4$ and $l_{int} = 2$. The energy gap separation losses to the intermediate channels are negligible.

We find, in addition, that moving E_{int} has little effect on the rate constants for loss to channel f.

In this model, we use the threshold separation instead of magnetic field because that is the essential effect of the field, to shift incident and final thresholds relative to each other. We have chosen E_f to vary over the range similar to the effect of changing the field from 0 to 1000 Gauss for the dominant zero-field loss channel, $|10-\rangle|22-\rangle$.

Figure 4.4 shows the inelastic rates computed within this model. This three-channel model does a reasonable job of mimicking the prominent features of the full calculation, including the eventual and lasting decrease in rates as the states are separated in energy. In addition, the g-wave rates decay more slowly as a function of field than do the d-wave rates, which is consistent with the full calculation (compare Fig. 4.3). The declining values of the rate constant cannot, however, be attributed to a simple overlap integral of the form of Eq. (4.1), since the incident and final channels are not directly coupled. We therefore present a more refined adiabatic analysis of this process in the next subsection.

4.1.3 Adiabatic Analysis of the Magnetic Field Case

To understand the system's magnetic field behavior we analyze the reduced channel model (4.2) in the adiabatic representation discussed in Sec. 3.6.

A partial set of adiabatic potential curves generated in this way is shown in Fig. 4.5, and exhibits an avoided crossing at $R = 150$. Thus molecules incident on the uppermost channel scatter primarily at large values of R. This point has been made in the past when an electric field is applied [87]; here we note that it is still true in zero electric field and that scattering calculations can proceed without reference to short-range dynamics.

The result of the ADWBA is shown in Fig. 4.6. The two curves are for d (black) and g-wave (red) inelastic channels. Several key features are present that also occur in

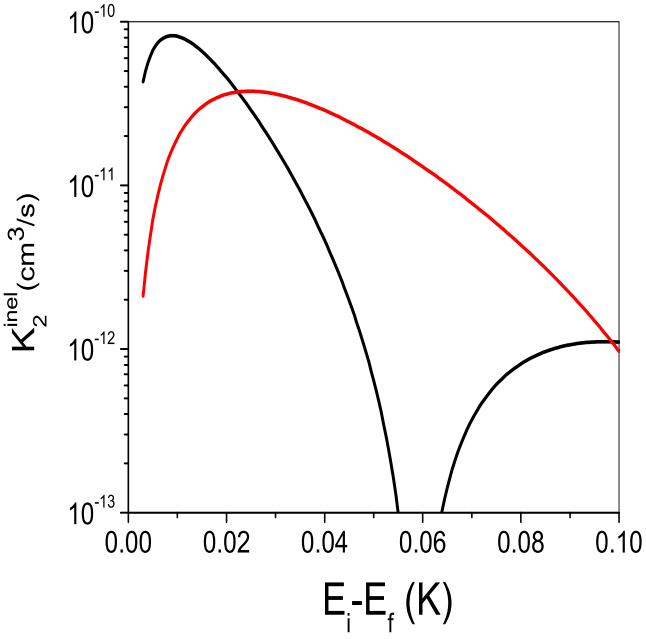

Figure 4.4: Inelastic rate constants for the three-channel model system, Eq. 4.2, as function of initial and final threshold separation. The two curves are for d and g-wave exit channels (black and red, respectively). In the g-wave channel, K_2^{inel} evolves more slowly as the thresholds are separated. The threshold separation shown corresponds to varying a magnetic field from 0 to 1000 Gauss for the dominant loss channel, $|10-\rangle|22-\rangle|22\rangle$.

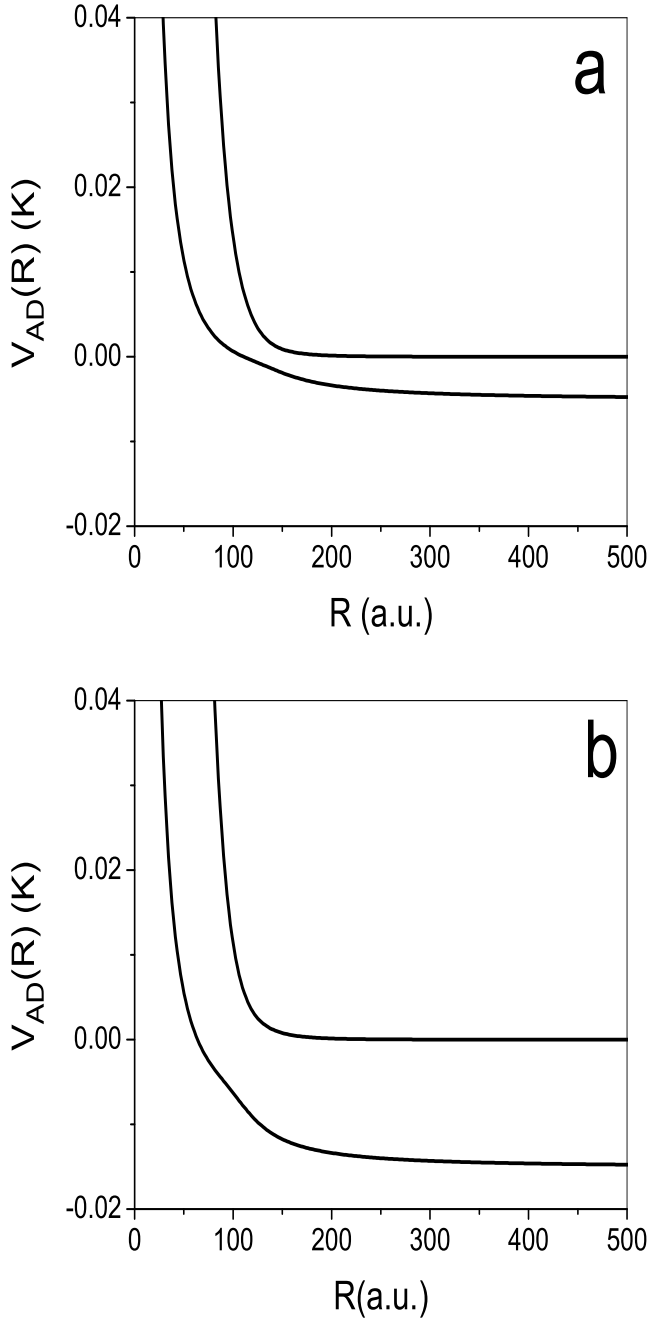

Figure 4.5: The relevant adiabatic potential curves for the OH-OH system. Shown are two different values of the final threshold energy $E_i - E_f = 5mK$ (a) and $E_i - E_f = 15mK$ (b)

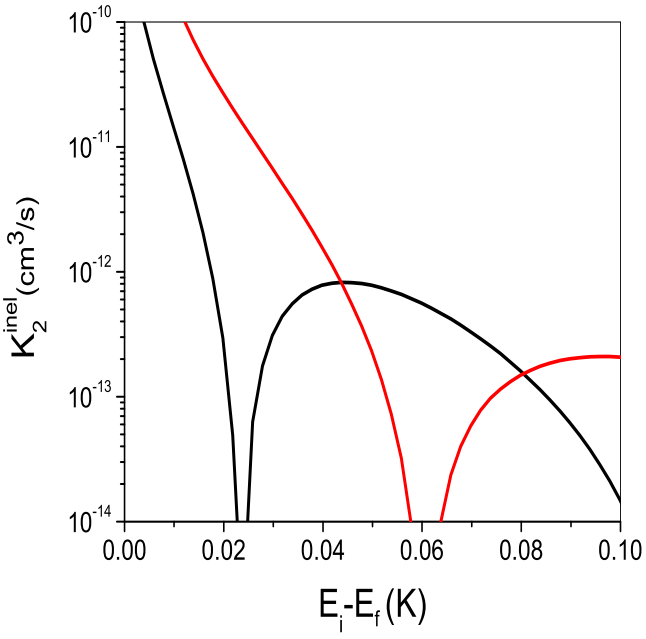

Figure 4.6: Inelastic rate constants as estimated by the adiabatic distorted wave Born approximation for the three-channel system. The black curve is for a d-wave exit channel, and the red for a g-wave exit channel. The threshold separation shown corresponds to varying a magnetic field from 0 to 1000 Gauss for the dominant loss channel, $|10-\rangle|22-\rangle$.

the full calculation, namely: (1) the inelastic rate goes down with increasing threshold separation, (2) there is a zero in the rates, as seen in Fig. 4.3, and (3) the g-wave inelastic rate goes more slowly than the d-wave, as seen in the model and the full calculation. The ADWBA accounts for all of these. The first feature, diminishing rates, still arises from an energy gap suppression, since the de Broglie wavelengths of incident and final channel still do not match well. In the ADWBA, this process is further helped along by the fact that the residual channel coupling, represented by P, is localized near the avoided crossings of the adiabatic potential curves.

The ADWBA helps to visualize this suppression, as shown by the sample wave functions in Fig. 4.7. This figure shows ψ_ι, $\frac{d}{dR}\psi_\varphi$, and $P_{\iota\varphi}$ for various values of E_f. Varying E_f mimics the shift of the thresholds in an applied magnetic field. The values of E_f of Fig. 4.7 are (a) $E_f = -6mK$, (b) $E_f = -22mK$, and (c) $E_f = -62mK$. The effect of the different E_fs leave ψ_ι mostly unchanged. However, ψ_φ becomes more exothermic and therefore more oscillatory (λ_{db} clearly shortens). Moreover, the dominant coupling region where $P_{\iota\varphi}$ peaks moves to shorter R as E_f increases. This motion is obvious from the avoided crossing in Fig. 4.5.

The transition amplitude in the ADWBA given in Eq. (3.39) is proportional to the integral of the product of the three quantities in Fig. 4.7. Because of the shortening of the de Broglie wavelength in the exit channel, this integral will eventually vanish, accounting for the zero in the inelastic rates. The *total* rate will, in general, not vanish, since there are many exit channels, and they will experience destructive interference at different values of the threshold, hence at different fields.

Finally, the g-wave inelastic rates are not so strongly affected by the separation of E_i and E_f because the g-wave centrifugal barrier is larger, meaning a greater energy is required to change the wave function at short range such that a node in the velocity can pass through the coupling region. The zero in this rate constant will thus occur at larger threshold separations.

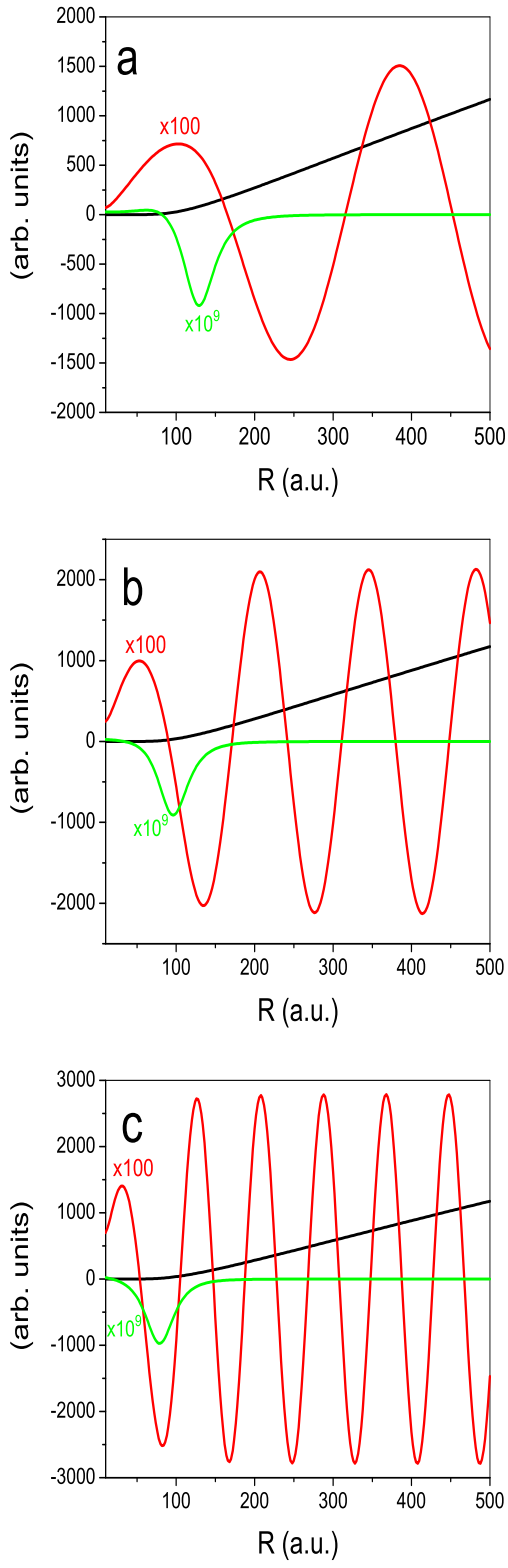

Figure 4.7: Illustrations of the origin of the zero in the partial rates. Each panel shows curves ψ_ι, $\frac{d}{dR}\psi_\varphi \times 100$ and $P_{\iota\varphi}$ $\times 10^9$. The plots are for different final energies, and the inelastic rate from the Born approximation are (a) $E_f = -6mK$ and $K_{\iota\varphi}^{inel} = 5\times10^{-11}(cm^3/s)$, (b) $E_f = -22mK$, $K_{\iota\varphi}^{inel} = 5\times10^{-14}(cm^3/s)$, and (c) $E_f = -62mK$, $K_{\iota\varphi}^{inel} = 6\times10^{-13}(cm^3/s)$, see text for details.

4.2 Conclusions

We have explored the influence of a magnetic field on the cold collision dynamics of polar molecules. The dipole-dipole interactions remain significant even in the absence of an electric field that polarizes the molecules. In general, this implies that molecular orientations are unstable in collisions, making magnetic trapping infeasible. We have found, however, that a suitably strong magnetic field can mitigate this instability.

Beyond this result, we note that laboratory strength fields can exert comparable influence on cold collisions, if applied separately. A useful rule of thumb in this regard is that an electric field of 300 V/cm acting on a 1 D dipole moment causes roughly the same energy shift as a 100 Gauss field acting on a 1 Bohr magneton magnetic moment. This raises the interesting question of how the two fields can be applied simultaneously to exert even finer control over collision dynamics. This will be the subject of future investigations.

Chapter 5

Strong-Field Seekers and the Influence of an Electric Field

Conventional spectroscopy of atoms and molecules begins with the premise that the energy levels of the species being probed are fixed even though they may shift slightly in electromagnetic fields. These levels are then interrogated by energy-dependent probes such as photons or charged or neutral particles. Information on the energetics and structure of the molecules is extracted from absorption energies, oscillator strengths, selection rules, etc. In these investigations, the study of resonances has played a central role.

With the advent of ultracold environments for atoms and molecules, this general view of spectroscopy can be inverted. Cold collisions provide a nearly monochromatic probe of near-threshold intermolecular interactions, with resolution set by the milli-Kelvin or micro-Kelvin temperature of the gas. In this case, the energy levels of nearby resonant states can be tuned into resonance with the zero-energy collisions. For cold gases of alkali atoms, this strategy is already in widespread use. It exploits the fact that the Zeeman effect can shift the internal energies of the atoms over ranges orders of magnitude larger than the collision energy itself. In this way, atoms can be made to resonate when they would not naturally do so (i.e., in zero field). Measurement of these "Feshbach" resonances (more properly, Fano-Feshbach resonances) has yielded the most accurate determination of alkali-alkali potential energy surfaces for near-threshold processes [113].

The current experimental and theoretical push to create and study ultracold molecules [30] will lead to many more opportunities for this novel kind of spectroscopy, since molecules possess many more internal degrees of freedom than do atoms. There will be, for example, numerous Fano-Feshbach resonances in which one or both of the collision partners becomes vibrationally or rotationally excited [71, 114, 115]; statistical arguments suggest that these resonances will be quite narrow in energy, a fact related to their abundance [114]. A second class of resonant states will occur when the constituents are excited into higher-lying fine structure or hyperfine structure states, more reminiscent of the resonances observed in alkali atoms. In molecules, these resonances are naturally also tunable in position using magnetic fields [116].

In this chapter, we are primarily interested in a third class of resonance: potential resonances that are engendered by altering the intermolecular potential energy surface itself. This capability becomes especially prominent in cold collisions of heteronuclear polar molecules, whose dipolar interactions are quite strong on the scale of the low translational temperatures of the gas. At the same time, the dipole moments of the individual dipoles can be strengthened or weakened as well as aligned by an applied electric field.

This kind of resonance includes shape resonances, discussed in the context of cold atoms polarized by strong electric fields [117, 118]. A second set dubbed "field-linked" resonances has been studied in some detail in Refs [90, 87, 91]. These states appear in PES's that correlate to weak electric field-seeking states of free molecules. They are weakly bound, long-range in character, and indeed do not appear to exist without an electric field present. Similar resonances are predicted to occur in metastable states of the alkaline earth elements at low temperatures [119, 120].

A rich set of potential resonances emerges among strong-field seeking states, and this is the subject of the present paper. Strong-field seekers are of increasing importance experimentally, since they enable molecules to be trapped in their absolute ground

states where no two-body inelastic collision processes are available to harm the gas. In this case, the colliding molecules are free to approach to within a small internuclear distance of one another; the resulting potential resonances therefore can probe detailed intermolecular dynamics near threshold. The resulting data, consisting of scattering peaks as a function of electric field, can be thought of as a kind of "Stark spectroscopy." Just such a tool has been applied previously in precision measurements of alkali Rydberg spectra [121, 122].

In this chapter, we explore such spectra in ultracold molecules, finding that the spectrum is dominated by a quasi-regular series in the electric field values. Such a series is the fundamental building block of molecular Stark spectroscopy and plays a role analogous to the Rydberg series in atomic spectroscopy. In both cases, the series lays out the fundamental structure of the unperturbed, long-range physics between interacting entities. In the case of atoms, the *deviation* from an unperturbed Rydberg series, encapsulated in the quantum defects, yields information on the electron-core interaction [123, 124]. Similarly, it is expected that differences in observed Stark spectra from those presented here will probe the short-range intermolecular interactions.

Using this formalism, introduced in section 2, we study the potential resonances using a simplified version of the molecular gas in which all dipoles are assumed to be perfectly aligned and where molecular fine structure plays no role. In Sec. IV, we consider the case of more realistic molecules, where fine structure does intervene. We show that the structure of the potential resonances is unchanged, but that additional narrow Fano-Feshbach resonances do appear. Throughout this chapter, we emphasize how the various types of resonance can be classified and organized by simple considerations involving the WKB approximation. To introduce the ideas, we first illustrate them with a simple "toy" model of pure polarized dipoles.

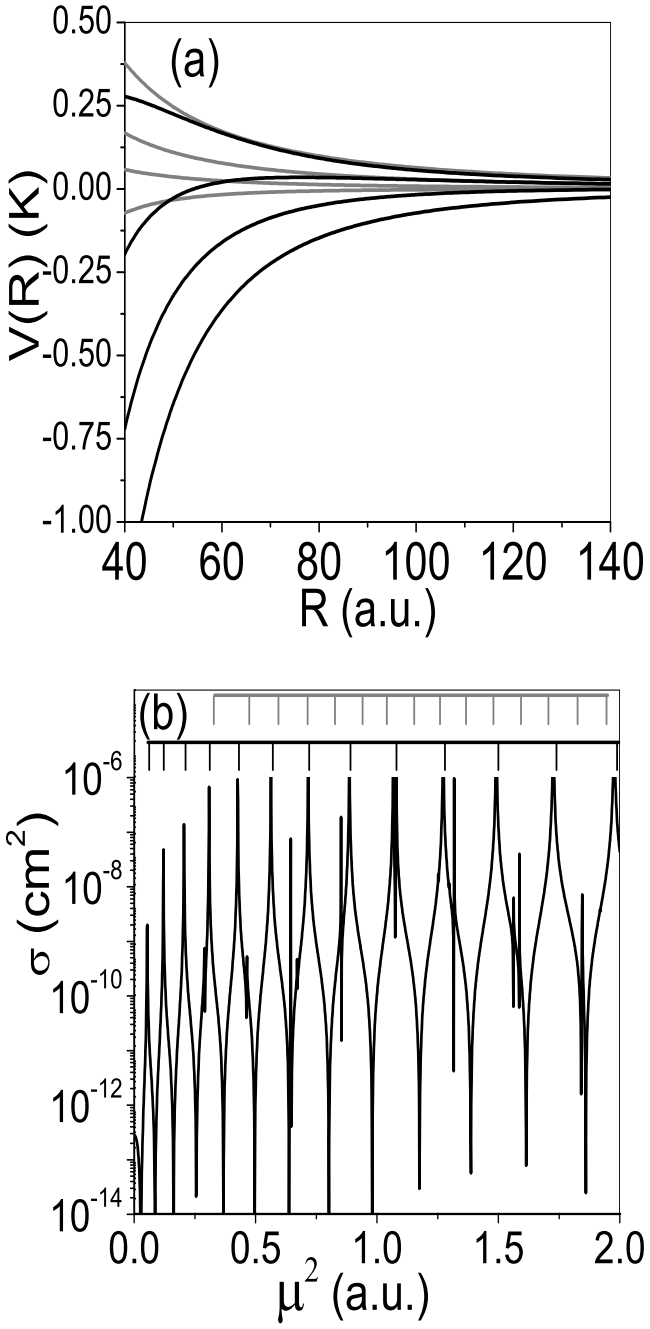

Figure 5.1: (a) Adiabatic curves of the pure dipole system for two values of the dipole moment μ: $\mu = 0.1$ (gray) and $\mu = 1$ (black) (b) The cross section of the polarized dipole model versus μ, at a collision energy $E = 10^{-12}$ K. The brackets denote predicted resonant positions using the adiabatic WKB phase (AWP) approximation. The black bracket represents the phase contribution from the lowest adiabatic curve, and the gray is from all remaining contributions.

5.1 Dipolar Scattering

Our primary interest in polar molecule scattering is how the strong anisotropic interaction affects the system. As a first step illustrating the influence of dipolar interactions, we present a simple model composed of polarized dipoles with no internal structure. Strictly speaking, this system is created by an infinitely strong electric field that completely polarizes the molecules and raises all other internal states to experimentally unattainable energies. Thus the only label required for a channel is its partial wave, $l = \{0, 2, 4, ...\}$ in the numerical example given here. The matrix elements of the dipole-dipole interaction are taken to be $\langle 12l0|H_{\mu\mu}|12l'0\rangle = -0.32\mu^2\langle l0|C_0^2|l'0\rangle$, which is typical for molecules like RbCs or SrO. We then artificially vary the dipole moment μ to see the effect of an increasingly strong dipolar interaction. Pragmatically speaking, varying μ parallels changing the electric field. The intention of this model is to focus on the effect of direct anisotropic couplings between the degenerate channels, as measured by their effect on the partial wave channels.

For this model, we use a reduced mass of $m_r = 10^4$ a.u., typical of very light molecules. We moreover assume that the molecules approach one another along the laboratory z-axis, so that only the projection $m_l = 0$ of orbital angular momentum is relevant. To set a concrete boundary condition at small R, we apply "hard wall" boundary conditions, $\psi(R_{in}) = 0$ at a characteristic radius $R_{in} = 20$ a.u. We pick the collision energy to be nearly zero, namely 10^{-12} K. To converge the calculation for this model requires inclusion of partial waves up to $l = 14$ and numerical integration of the Schrödinger equation out to $R = R_\infty = 1 \times 10^5$ a.u. using the log-derivative propagator method of Johnson [108].

To get a sense of the influence of increasing the dipole moment, we first look at adiabatic curves of the system. Figure 5.1 (a) shows two different sets of adiabatic curves: a gray set with $\mu = 0.1$ (a.u.) and a black set $\mu = 1.0$ (a.u.). In each set, the four

lowest adiabatic curves are shown. Looking at these curves, we can see two characteristic effects of increasing μ. First, the lowest curve becomes much deeper. Second, the higher adiabatic curves, originating from nonzero partial waves, may support bound states at short distance states, i.e., within the centrifugal barrier. Both these effect may generate bound states, leading to distinct classes of scattering resonances as μ is varied. The deepening of the lowest adiabatic curves induces potential resonances, whereas the higher-lying curves lead to narrow shape resonances wherein the molecules must tunnel through the centrifugal barrier.

The different classes of resonances can clearly be seen in cross section, in Fig. 5.1 (b). The broad quasi-regular set of resonances seen in the cross section are the potential resonances originating from the lowest adiabatic curve. The narrow shape resonances appearing sporadically in the spectrum originate from the higher-lying curves. For the purpose of this chapter, we focus on the wide potential resonances and simply acknowledge the existence of the narrow shape resonances.

To show that the broad resonances primarily belong to the lowest potential and the narrow shape resonances belong to the higher-lying potentials, we use an eigenphase analysis. The eigenphase can be thought of as the sum of the phase shifts for all of the channels; thus it tracks the behavior of all the channels simultaneously. The eigenphase is defined as

$$\phi_{eigen} = \sum_i \tan^{-1}(\lambda_i^K). \tag{5.1}$$

Here λ_i^K are the eigenvalues of the K matrix from the full-scattering calculation [104]. The K matrix is related to the more familiar scattering matrix by $S = (1+iK)/(1-iK)$. When the system gains a bound state, it appears as a π jump in eigenphase. The eigenphase of the system is shown in Fig. 4.2 (a) as the solid line with many abrupt steps.

To analyze this situation further, we construct an approximate eigenphase as

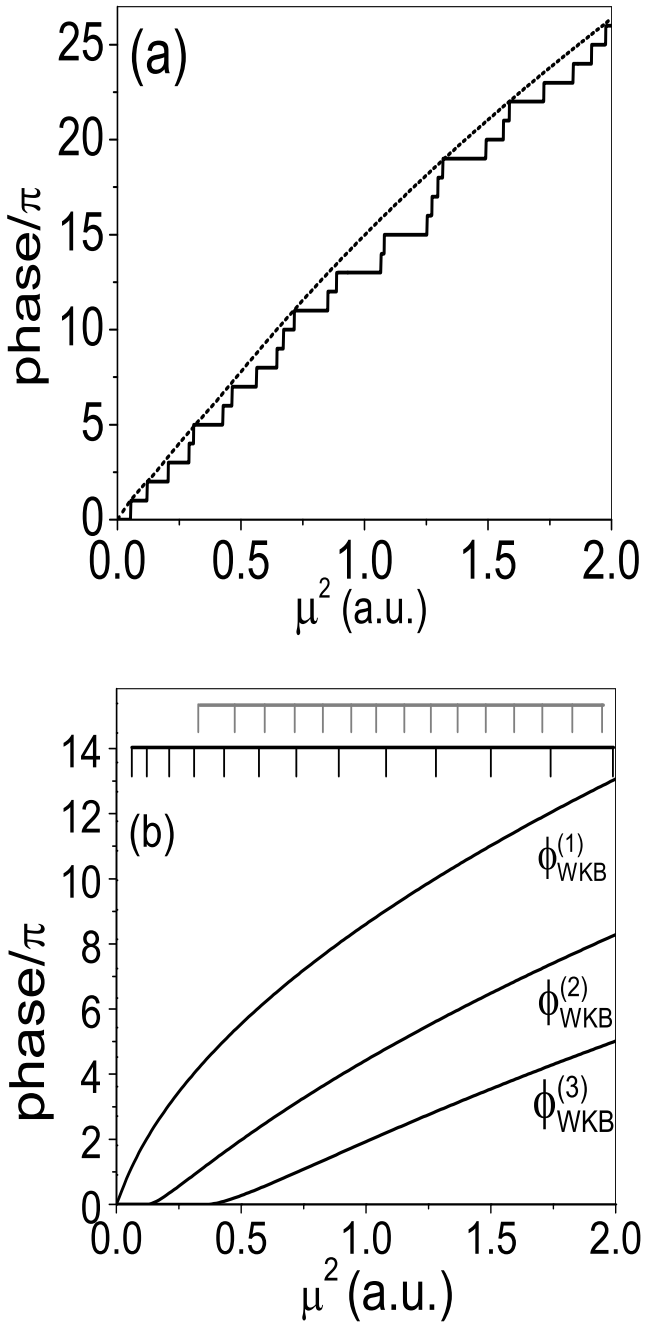

Figure 5.2: (a) Eigenphase (solid) and total adiabatic WKB phase (AWP, dashed) for the dipole-scattering model. (b) AWP contributions for the lowest adiabatic curves ($\phi^{(1)}_{WKB}$) with the black bracket indicating when $\phi^{(1)}_{WKB}$ passes through a multiple of π. The two remaining curves are contributions with nonzero partial waves ($\phi^{(2,3)}_{WKB}$). The gray bracket indicates where the sum of these contributions passes through a multiple of π.

follows. First, we assess the total phase accumulated in each adiabatic channel using a WKB prescription:

$$\phi^{(i)}_{WKB}(\mu) = \int_{R_{in}}^{R_{out}} \sqrt{-2m_r V^{(i)}_{AD}(\mu, R)/\hbar^2}. \tag{5.2}$$

Here (i) stands for the i^{th} adiabatic curve. For the lowest adiabatic curve, which is always attractive, the range of integration is from R_{in} to $R_{out} = \infty$. For high-lying channels that possess a barrier to scattering at zero collision energy, the limits of integration are from R_{in} to the inner classical turning point of the barrier. This will yield some information on shape resonances trapped behind the barrier, but we will not make much of this in the analysis to follow. Finally, we add together the individual WKB phases to produce an approximate eigenphase shift, which we dub the "adiabatic WKB phase" (AWP):

$$\phi_{WKB}(\mu) = \sum_i \phi^{(i)}_{WKB}(\mu). \tag{5.3}$$

Since we are not concerned with properties of the phase associated with the higher-lying adiabatic curves, we do not consider the connection formula now.

The total AWP for this system is shown as a dashed line in Fig. 5.2 (a). It tracks the eigenphase well but offers more information if we decompose the AWP into its contributions. Figure 5.2 (b) shows the individual contributions of the sum. The largest contribution is the phase from the lowest adiabatic curve, which can be associated with potential resonances. A black bracket appears above this phase contribution with vertical marks indicating when it passes through an integer multiple of π, i.e., when we expect to see a potential resonance in the cross section. This same bracket is plotted in Fig. 5.1 and shows good agreement between the locations of the potential resonances and the AWP predictions. We conclude from this that the main resonance features in the Stark spectrum arise primarily from this single potential curve.

In Fig. 5.2 (b), the two remaining phase contributions originate from nonzero partial wave channels that possess centrifugal barriers; see Fig. 5.1(b). The gray bracket

indicates where the sum of these two contributions passes through an integer multiple of π, and thus represents a guess for where the shape resonances lie. This gray bracket is also shown in Fig. 5.1. The agreement with the position of the narrow resonance features in the cross section is not nearly as good as it is with the broad potential resonances. This indicates a more involved criterion for shape resonances. Nevertheless, the AWP predicts 15 shape resonances, and there are 13 in the range of μ shown. The AWP appears to offer a means to roughly predict the number of shape resonances in this system, even though it does not predict the locations exactly.

A main point of this analysis is that the AWP in the lowest adiabatic channel that alone is sufficient to locate the potential (as opposed to shape) resonances without further modification. For the rest of this chapter, we focus on the potential resonances in more realistic molecules with internal molecular structure. The general analysis in terms of a single-channel AWP will still hold, but an additional phase shift will be required to describe the spectrum.

5.2 Strong-Field Seekers

Strong-field-seeking molecules are approximately described as polarized in the sense of the last section, because their dipole moments are aligned with the field. They will, however, contain a richer resonance structure owing to the presence of low-lying excited states that can alter the dipolar potential energy surface at small R.

For concreteness, we focus here on molecules with a $^1\Sigma$ ground state. Heteronuclear alkalis fit into this category and are rapidly approaching ground state production with various species [125]. As examples, we pick RbCs and SrO in their ground states. Ground state RbCs has been produced experimentally [49]. As for SrO, promising new techniques should lead to experimental results soon [126]. For simplicity we include only the $J = 0$ and $J = 1$ rotational states and freeze the projection of molecular angular momentum to $M_J = 0$. This restricts the number of scattering thresholds to three,

identified by the parity quantum number of the molecules in zero field. The parity quantum numbers for the three thresholds are $(--, -+, ++)$. This model is similar to the one presented in Ref. [87] that can be easily constructed for any rigid rotor when only including two molecular states. One immediate consequence of multiple thresholds is the presence of rotational Fano-Feshbach resonances in the collisional spectrum.

The first example is RbCs, whose physical parameters are $\mu = 1.3$ D, $m_r = 110$ a.m.u., and $B_e = 0.0245(K)$ [49]. As before, we apply a vanishing boundary condition at $R_{in} = 20$ a.u. To converge this calculation over the field range considered, we require partial waves up to $l = 30$. We first look at the adiabatic curves of the system to get an understanding of how the real system deviates from the simple model presented above. In Fig. 5.3 (a), we plot the six lowest adiabatic curves for the RbCs system with only four partial waves, so the figure is more easily interpreted. The sets of adiabatic curves shown are for two different field values: the gray set has $\mathcal{E}$=0 and the black set has $\mathcal{E}$= 5000 (V/cm). There are two important features that differ from the dipole example. First, there are two higher thresholds, and the electric field shifts these apart in energy as the field is increased. Second,the electric field dramatically changes the radial dependence of the Hamiltonian.

The difference in thresholds can be seen clearly in Fig. 5.3 (a) where the lowest excited threshold moves from $0.05(K)$ at $\mathcal{E}$=0 to $0.18(K)$ at $\mathcal{E}$=5000 (V/cm). The difference in radial dependences for the two cases is seen more clearly in a log-log plot of the two lowest adiabatic curves for both fields, as shown in Fig. 5.3 (b). The gray set corresponding to zero field has two distinct asymptotic radial powers. At large R, the lowest adiabatic curve has a $1/R^6$ behavior asymptotically because of couplings with channels far away in energy [$\sim 0.05(K)$]. However as R approaches zero, the dipolar interaction has overwhelmed the rotational energy separation, and the radial dependence becomes $1/R^3$ in character at about R=100 (a.u.). For reference, the dashed line is proportional to $1/R^3$. With $\mathcal{E}$= 5000 (V/cm), the two black curves show the radial

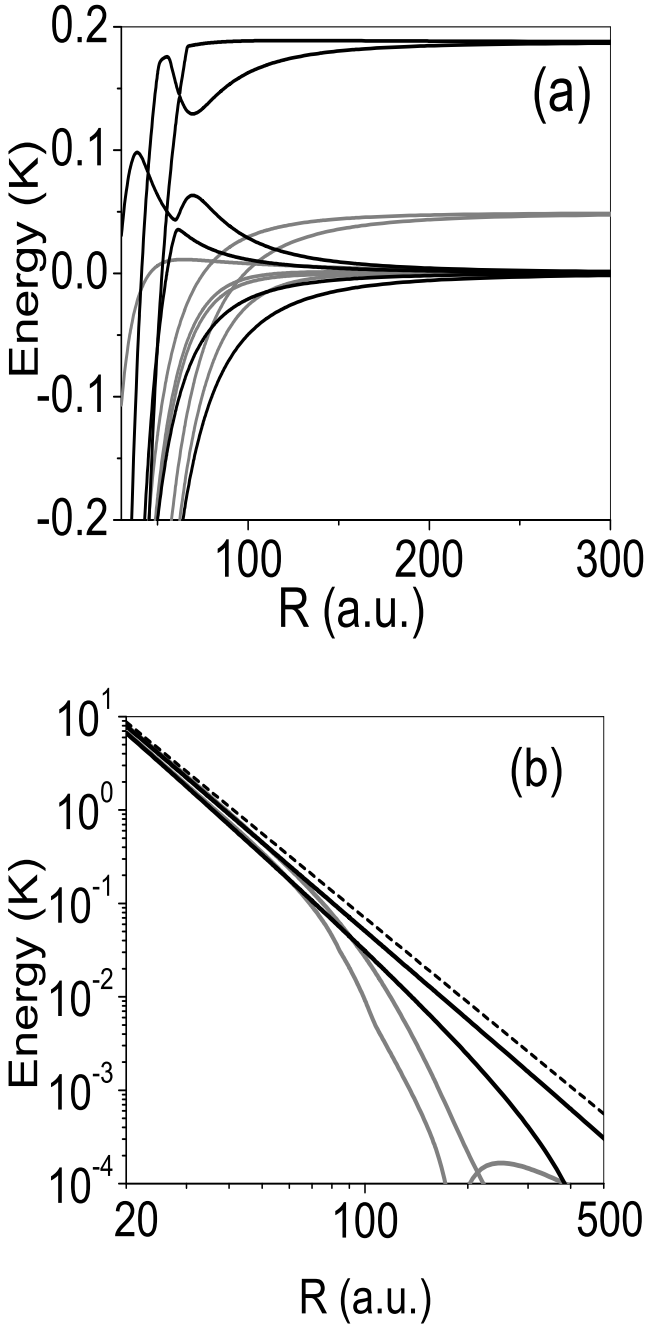

Figure 5.3: (a) Adiabatic curves for the RbCs system at two different field values, $\mathcal{E} = 0(V/cm)$ (gray) and $\mathcal{E} = 5000(V/cm)$ (black). (b) Log-log plot of the absolute value of the two lowest adiabatic curves. The blue dashed line is proportional to $1/R^3$.

dependence of the adiabatic curves. The lowest curve now has nearly $1/R^3$ behavior over the whole range shown. Asymptotically when the centrifugal barrier is larger, the radial dependence will change to $1/R^4$ [87]. The second lowest adiabatic curve is also significantly altered by the strong dipolar interaction as can be seen in Fig. 5.3 (b).

In Fig. 5.4 (a), we plot the cross section for the model RbCs system. This spectrum is riddled with narrow Fano-Feshbach resonances but is still dominated by a series of potential resonances similar to the one in Fig. 5.1 (b). There are two sets of AWP predictions shown as over-brackets. To understand their difference, we look to Fig. 5.4 (b). The AWP for the lowest adiabatic curve is shown in Fig. 5.4 (b) for two different zero-field phase values. The gray curve is the AWP that is directly computed from the method described in Eq. (5.3). The locations where it passes through an integer multiple of π are indicated by the gray triangles. Referring back to Fig. 5.4 (a), where the same gray triangles appear, we see that this simple estimate does *not* reproduce the resonance position.

We can, however, introduce an additional overall phase shift to account for the difference in short-range interactions from the pure polarized case. The shifted AWP reads

$$\tilde{\phi}^{(1)}_{WKB}(\mathcal{E}) = \phi^{(1)}_{WKB}(\mathcal{E}) + \pi\delta_{defect}. \tag{5.4}$$

By treating δ_{defect} as a fitting parameter, we can obtain the resonance positions indicated by the black bracket in Fig. 5.4, which agree quite well with the resonance positions in the close-coupled calculation. To do so requires, in this case, a phase shift $\delta_{defect} = 0.14$. In analogy with Rydberg spectroscopy, we consider the shift we have added to be a "quantum defect" that accounts for the effect of the short-range interaction. The additional phase shift reflects the influence of short-range physics on the scattering such as curve crossings with curves from higher thresholds.

The AWP also saturates with field, as can be seen in Fig. 5.4 (b). This saturation

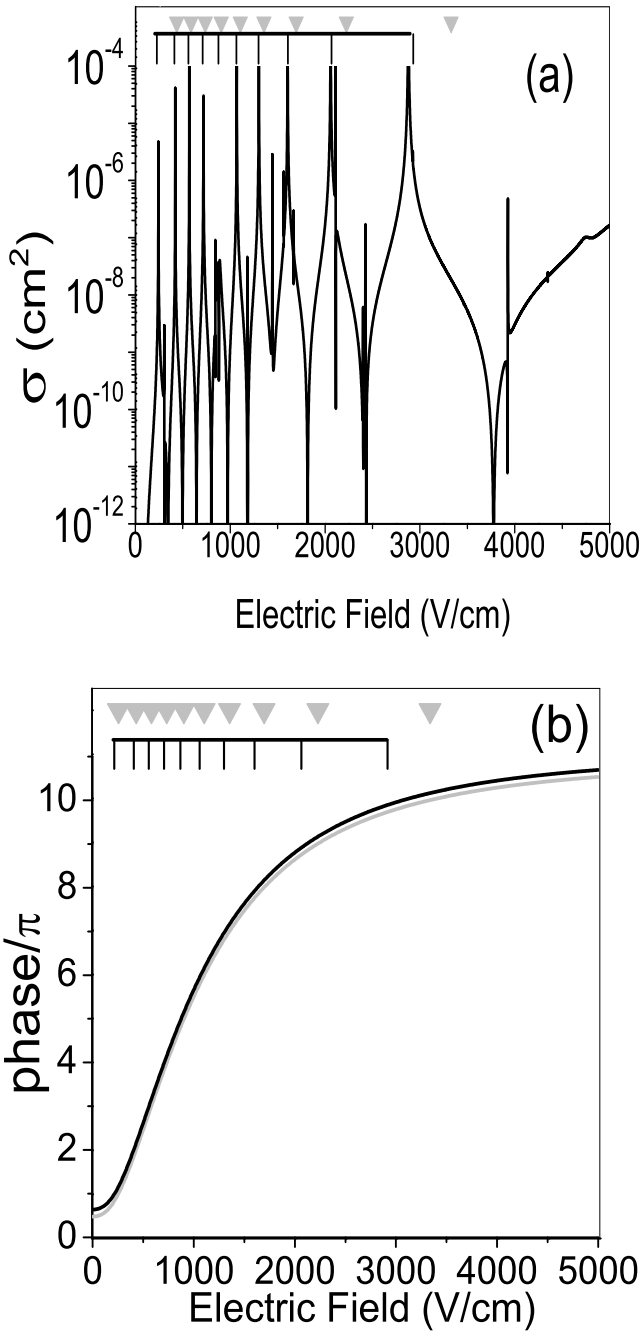

Figure 5.4: (a) Cross section for RbCs in strong-field seeking states, including the 10 potential resonances that the AWP predicts (solid bracket). The AWP phases are shown in (b). The black bracket corresponds to the AWP predicted resonances for the lowest adiabatic curve after a defect, $\delta_{defect} = 0.14$, has been added according to Eq. (5.4). The gray triangles are the AWP predicted resonances without the defect.

occurs because the electric field eventually fully polarizes the molecules, so the dipole moment cannot increase further. The effect can also be seen in the spacing of the potential resonances. At low fields, the potential resonances occur frequently in field. Then, as the field is further increased, the resonances occur less often in field, which is a signature of dipole moment saturating and therefore an increasing field having less effect on the molecular interaction.

As a second example, we consider SrO, which has the physical parameters m_r=52 a.m.u, μ=8.9 D, and $B_e = 0.5$ K [39]. We choose this molecule for its comparatively large mass and dipole moment, which guarantee a large number of resonances. In Fig. 5.5 we have plotted the cross section for SrO, which is dominated by the quasi-regular potential resonance series. As before, the black bracket indicates where the phase shifted, AWP predicts the potential resonances, and we see the agreement is good. Furthermore, the series has not terminated since we have not completely polarized the dipole. The series of potential resonances saturates at 17.5 (kV/cm) after a total of 43 potential resonances have been induced. To line up the AWP's predictions and the actual cross section requires a defect of $\delta_{defect} = 0.215$.

We have picked two examples to illustrate how the potential resonances will appear in the context of collisional spectroscopy. These resonances will occur to varying degrees in the strong-field seeking collisions of all polar molecules. For example, we can also make similar predictions for an asymmetric rotor molecule such as formaldehyde (H_2CO). We find that this molecule should possess six potential resonances in the field interval from 0 to 50 kV/cm.

It is worth noting that portions of similar resonance series were anticipated in cold atomic gases subjected to electric fields [118]. However very few such resonances are likely to be observed, owing to the enormous fields $\sim MV/cm$ required to generate them. In polar molecules, by contrast, the entire series should be readily observable.

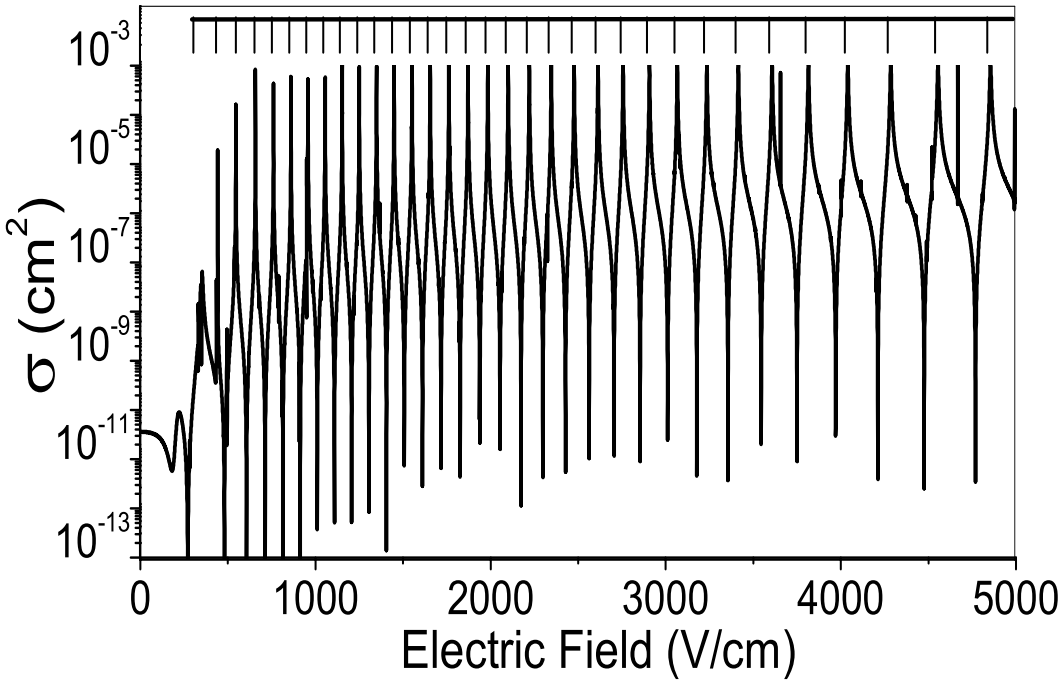

Figure 5.5: Cross section for SrO with a bracket indicating resonance positions predicted by the phase shifted AWP for the lowest adiabatic curve. There are 33 PR shown in this range of electric field. $\delta_{defect} = 0.215$.

5.3 Collisional Spectroscopy

Through the course of this work, we have shown that the zero-energy cross section of strong-field-seeking molecules is dominated by a set of broad potential resonances. Even though these resonances are themselves intriguing, their properties can be exploited to learn much more about the system. The general structure of the potential resonances is governed by the long-range dipolar interaction, which has a predictable and common form. With a clear understanding of this interaction and how it induces resonances, it could be exploited to learn about the short-range interaction of the molecules. This is because details of where the lines appear must also depend on the boundary condition experienced by the wave function at small values of R. Therefore the spectrum contains information on the small R intermolecular dynamics. Thus by studying the potential resonance series, we can extract information about the short-range dynamics.

This idea is similar to quantum defect theory, which has been very successful in the spectroscopy of Rydberg atoms. The short-range physics of the electron interacting with the nucleus is complicated and not easily solved. However, once the electron is out of the small R region, it enters into a pure coulomb potential where its motion is well understood. The effect of the short range must be merged with long-range physics to form a complete solution. To account for the short-range interaction, the energy can be parameterized by replacing the principal quantum number with an effective quantum number $n^\star = n - \mu$. This procedure is tantamount to identifying an additional phase shift due to the interaction of the electron with the atomic core. The idea of merging standard long-range physics with complicated short-range behavior has been applied successfully not only in Rydberg states of atoms [124, 127] and molecules [128], but also in atomic collisions [129], cold collisions [131, 132, 130], and dipole-dipole interactions of the type we envision here [118].

As a simple expression of this idea, we can alter the boundary condition applied

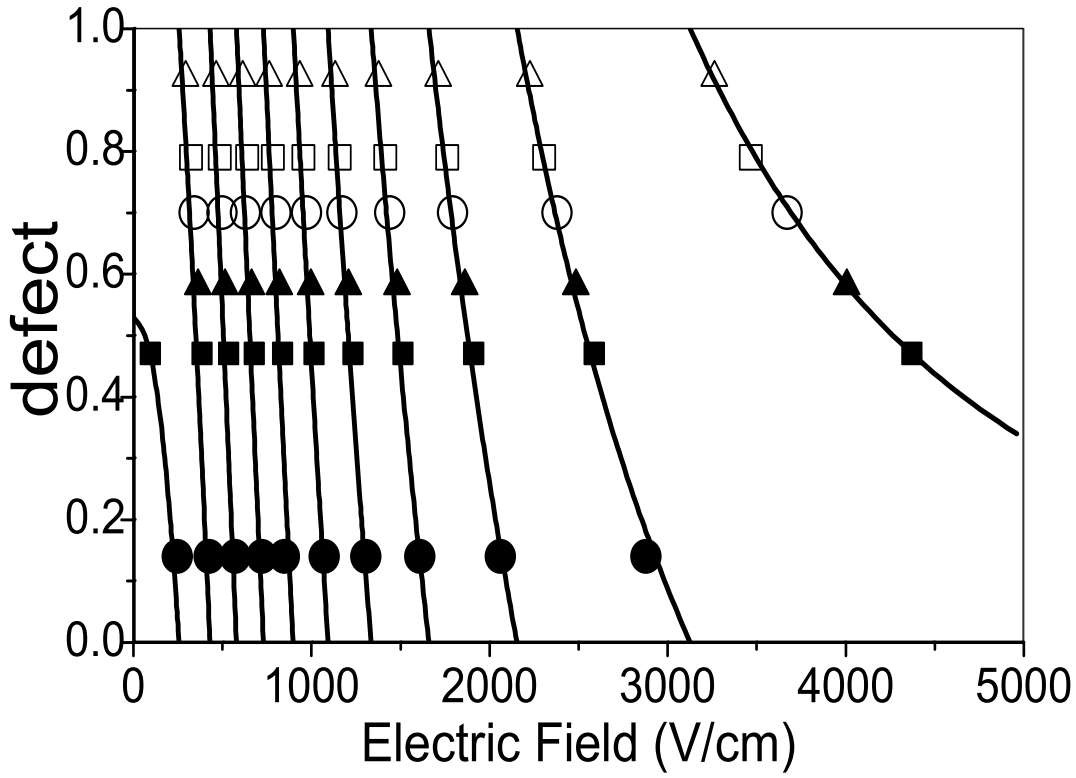

Figure 5.6: The vertical curves represent electric field values where the AWP predicts potential resonances for a given defect, $\mathcal{E}_{WKB}(\delta_{defect})$. The points represent resonant field values, $\mathcal{E}^{(b)}$, in the full calculations with different initial boundary conditions. The values of b are given by cotan$(\pi\beta)$. The values of β for the different full numerical calculations are 0 (filled circle), 0.11 (filled square), 0.22 (filled triangle), 0.56 (hollow circle), 0.78 (hollow square), and 0.89 (hollow triangle). Each set of values $\mathcal{E}^{(b)}$ is plotted at a height corresponding to its best-fit value of δ_{defect}.

at R_{in} when performing the full scattering calculation and note its influence on the field dependent spectrum. For the above calculations, we have imposed the standard vanishing boundary condition, $\psi(R_{in}) = 0$, for all channels. We now replace this condition with a uniform logarithmic derivative, $b = (\frac{d}{dR}\psi)\psi^{-1}$, at R_{in}. Thus previously we set $b = \infty$, but now we allow b to vary. The log-derivative is conveniently represented as a phase:

$$b = \text{cotan}(\pi\beta), \tag{5.5}$$

where β can lie between zero and one, covering all values of b from $-\infty$ to $+\infty$. For $\beta = 0$, the boundary condition is the one employed above, $\psi(R_{in}) = 0$, whereas for $\beta = 0.5$, the boundary condition is $\frac{d}{dR}\psi(R_{in}) = 0$.

We have recomputed the collisional spectrum of RbCs for several different initial conditions, and plotted the field values of the potential resonances, $\mathcal{E}^{(b)}$, in Fig. 5.6 as sets of points. The values of β for the different calculations are 0 (filled circle), 0.11 (filled square), 0.22 (filled triangle), 0.56 (hollow circle), 0.78 (hollow square), and 0.89 (hollow triangle). The filled circles are resonant locations for cross section in Fig. 5.4 (a).

We next wish to demonstrate that each such spectrum can be identified by a single quantum defect parameter, as was done in the previous section. This entails picking a value of δ_{defect} and then setting the phase $\tilde{\phi}^{(1)}_{WKB}(\mathcal{E})$ equal to an integer multiple of π. This yields a set of resonant field values, $\mathcal{E}_{WKB}(\delta_{defect})$. Each δ_{defect} corresponds to a particular approximate spectrum. The set of curves, $\mathcal{E}_{WKB}(\delta_{defect})$, generated by continuously varying δ_{defect} are shown are shown in Fig. 5.6 as solid lines. The bracket in Fig. 5.4 (a) corresponds to the set of points where a vertical line intersects $\mathcal{E}_{WKB}(\delta_{defect})$ with $\delta_{defect} = 0.14$.

We can compare the resonant field values predicted by the AWP, $\mathcal{E}_{WKB}(\delta_{defect})$, and resonant field values given by the full calculation with different initial conditions,

$\mathcal{E}^{(b)}$. To plot $\mathcal{E}^{(b)}$, we have varied the height at which the set of points $\mathcal{E}^{(b)}$ is plotted until it aligns with $\mathcal{E}_{WKB}(\delta_{defect})$. Doing this, we are able to to see how b and δ_{defect} are related. Thus in Fig. 5.6, we can see that even with different boundary conditions, the single AWP curve in Fig. 5.4 (b) can be used to predict the spacing between the potential resonances by varying a single parameter, δ_{defect}. This shows the AWP represents the long-range scattering physics well and that empirically extracted parameters like δ_{defect} will carry information about the short-range physics such as that embodied in b.

5.4 Conclusion

A number of resonant processes may occur when two polar molecules meet in an ultracold gas. We have focused here on the dominant, quasi-regular series of potential resonances between strong-field seeking states. These potential resonances originate in the direct deformation of the potential energy surface upon which the molecules scatter. Observation of these resonances may offer a direct means for probing the short range interaction between molecules. We have provided a means of analyzing this system with an adiabatic WKB phase integral. This method shows how the system evolves with the application of an electric field.

Chapter 6

The Last and Shortest Chapter

Throughout the course of this work, we have studied the effects of external fields on collisions of polar molecules. First, we explored how the use of a magnetic field could suppress inelastic loss rates for weak-field seeking states of OH. We used a simple numerical method with which the suppression could be understood in terms of energy gap suppression. Second, we began the exploration of collisions between strong-field seeking states in the presence of an electric field. We found a quasi-regular set of potential resonances as a function of the electric field. To analyze these resonances, we used a simple WKB approximation to the eigenphase and explored the nature of the potential resonances.

There are many possible future directions for this work. One is to further the understanding of how external fields can control long-range scattering such that the molecules approach short range a in determined manner. This would lead to the ability to systematically extract information about the short-range interaction of the molecules and even the possibility of controlling chemical reactions. Another possible direction is to explore the parameterization of the molecular scattering such that faithful representations of the two-body interaction may be inserted into many body theories.

Bibliography

[1] K. Takahashi *et al.*, Phys. Rev. E **58**, 7805 (1998).

[2] N. Tjandra and A. Bax, Science, **278**, 1015 (1997).

[3] J. H. Prestegard *et al.*, Chem. Rev. **104**, 3519 (2004).

[4] P. Mohn, *Magnetic Materials in the Solid State*, (Springer, New York, 2002).

[5] K. BeBell *et al.*, Rev. Mod. Phys. **72**, 225 (2000); D. B. Laks, S. H. Wei, and A. Zunger, Phys. Rev. Lett. **69**, 3766 (1992).

[6] A. Michal and R. Tycko, Phys. Rev. Lett. **81**, 3988 (1998).

[7] L. Li and A. P. Alivisatos, Phys. Rev. Lett. **90**, 97402 (2003).

[8] G. F. Mazenko, *Equilibrium Statistical Mechanics*, (John Whiley and Sons, New York, 2000).

[9] V. J. Emery *et al.*, Phys Rev. E. **56** 6120 (1997).

[10] B. P. Stojkovic *et al.*, Phys. Rev. Lett. **82** 4679 (1999).

[11] C. J. Olson Reichhardt *et al.*, Phys. Rev. Lett. **92** 16801 (2004).

[12] H. J. Kang *et al.*, Nature **423**, 522 (2003).

[13] J. W. Lynn *et al.*, Phys. Rev. Lett. **60**, 2781 (1988).

[14] M. Uehara *et al.*, Nature **399** 560 (1999).

[15] J. J. Weis, J. Phys. Cond. Mat. **15** S1471 (2003).

[16] S. H. L. Klapp, J. Phys. Cond. Mat. **17** R525 (2005).

[17] S. A. Kivelson *et al.*, Proc. Natl. Acad. Sci. **98**, 11903 (2001).

[18] S. M. Choi and J. W. Lynn, Phys. Rev. Lett. **87**, 107001 (2001).

[19] M. A. Kastner *et al.*, Rev. Mod. Phys. **70**, 897 (1998).

[20] S. Brush, Rev. Mod. Phys. **39**, 883 (1967).

[21] J. Weiner *et al.* Rev. Mod. Phys. **71**, 1 (1999).

[22] M. H. Anderson *et al.*, Science **269**, 198 (1995).

[23] K. B. Davis *et al.* Phys. Rev. Lett. **75**, 3969 (1995).

[24] C. C. Bradely *et al.*, Phys. Rev. Lett. **75**, 1687 (1995).

[25] F. Dalfovo *et al.*, Rev. Mod. Phys. **71**, 463 (1999).

[26] B. DeMarco and D. S. Jin, Science **285**, 1703 (1999).

[27] C. A. Regal, M. Greiner, and D. S. Jin, Phys. Rev. Lett. **92**, 040403 (2004).

[28] M. W. Zwierlein *et al.*, Phys. Rev. Lett. **92**, 120403 (2004).

[29] C. Chin *et al.*, Science **305**, 1128 (2004).

[30] For a recent review, see J. Doyle, B. Friedrich, R.V. Krems, and F. Masnou-Seeuws, European Physical Journal D **31**, 149 (2004).

[31] M. A. Baranov *et al.*, Physica Scripta, **T102**, 764 (2002).

[32] L. Santos *et al.*, Phys. Rev. Lett. **85**, 1791 (2000).

[33] S. Yi and L. You, Phys. Rev. A **61**, 041604(R) (2000).

[34] S. Yi and L. You, Phys. Rev. A **66**, 013607 (2002).

[35] S. Giovanazzi, D. O'Drell, and G. Kurizki, Phys. Rev. Lett. **88**, 130402 (2002).

[36] K. Goral, L. Santos, and M. Lewenstein, Phys. Rev. Lett. **88**, 170406 (2002).

[37] M. A. Baranov, M. S. Mar'enko, Val. S. Rychkov, and G. V. Shlyapnikov, Phys. Rev. A **66**, 013606 (2002).

[38] B. Damski *et al.*, Phys. Rev. Lett. **90**, 110401 (2002).

[39] D. Demille, Phys. Rev. Lett. **92**, 067901 (2002).

[40] E. A. Donley, N. R. Claussen, S. T. Thompson, and C. E. Wieman, Nature (London) **417**, 529 (2002).

[41] C. A. Regal, C. Ticknor, J. L. Bohn, and D. S. Jin, Nature **424**, 47 (2003).

[42] K. E. Strecker, G. B. Partridge, and R. G. Hulet, Phys. Rev. Lett. **91**, 080406 (2003).

[43] J. Cubizolles *et al.*, Phys. Rev. Lett. **91**, 240401 (2003).

[44] S. Jochim *et al.*, Phys. Rev. Lett. **91**, 240402 (2003).

[45] C. A. Stan, M. W. Zwierlein, C. H. Schunck, S. M. F. Raupach, and W. Ketterle, Phys. Rev. Lett. **93** 143001 (2004).

[46] S. Inouye, J. Goldwin, M. L. Olsen, C. Ticknor, J. L. Bohn, and D. S. Jin, Phys. Rev. Lett. **93** 183201 (2004).

[47] A. J. Kerman *et al.*, Phys. Rev. Lett. **92**, 033004 (2004).

[48] A. J. Kerman *et al.*, Phys. Rev. Lett. **92**, 153001 (2004).

[49] J. Sage *et al.*, Phys. Rev. Lett. **94**, 203001 (2005).

[50] M. W. Mancini, G. D. Telles, A. R. L. Caires, V. S. Bagnato, and L. G. Marcassa, Phys. Rev. Lett. **92**, 133203 (2004) .

[51] D. Wang *et al.*, Phys. Rev. Lett. **93**, 243005 (2004).

[52] J. Weinstein, R. deCarvalho, T. Guillet, B. Friedrich, and J.M. Doyle, Nature **395**, 148 (1998).

[53] C.L. Cesar, D.M. Silveira, M.G. Veloso, F. Zappa, and C.C. Rodegheri, Hydrogen Atom III, The international conference on Precision Physics of Simple Atomic Systems, edited by C.L. Cesar, S.G. Karshenboim, V.A. Shelyuto (2004).

[54] A. Peters, Quantum Gases International Workshop, p. 19 (2003).

[55] R. deCarvalho, N. Brahms, B. Newman, C. Johnson, L. Willman, J. M. Doyle, T. J. Greytak, and D. Kleppner, Hydrogen Atom III, The International conference on Precision Physics of Simple Atomic Systems, edited by C. L. Cesar, S. G. Karshenboim, V. A. Shelyuto (2004).

[56] H.L. Bethlem, G. Meijer, Int. Rev. Phys. Chem. **22**, 73 (2003).

[57] J. R. Bochinski, E. R. Hudson, H. J. Lewandowski, and J. Ye, Phys. Rev. A (submitted).

[58] E. A. Hinds, Phys. Scripta **T70**, 34 (1997).

[59] M. R. Tarbutt, H. L. Bethlem, J. J. Hudson, V. L. Ryabov, V. A. Ryzhov, B. E. Sauer, G. Meijer, and E. A. Hinds, Phys. Rev. Lett. **92**, 173002 (2004).

[60] H. Gould, Department of Energy, Basic Energy Science Contractor's Meeting, 2003.

[61] P. F. Barker, A. I. Bishop, R. Fulton, and M. N. Shneider, in ACS 2004 National Meeting Technical Program (2004).

[62] M. Di Rosa, ITAMP-CUA Workshop on Ultracold Polar Molecules, Cambridge, (2004).

[63] M. Gupta and D. Herschbach, J. Phys. Chem. A **103**, 10670 (1999).

[64] M. S. Elioff, J. J. Valentini and D. W. Chandler, Science **302**, 1940 (2003).

[65] S. A. Rangwala, T. Junglen, T. Rieger, P. W. H. Pinkse, and G. Rempe, Phys. Rev. A **67**, 043406 (2003).

[66] E. Nikitin, E. Dashevskaya, J. Alnis, M. Auzinsh, E.R.I. Abraham, B.R. Furneaux, M. Keil, C. McRaven, N. Shafer-Ray, and R. Waskowsky, Phys. Rev. A **68**, 023403 (2003).

[67] A. Volpi and J. L. Bohn, Phys. Rev. A **65**, 064702 (2002).

[68] P. Soldan *et al.*, Phys. Rev. Lett. **89**, 153201 (2002).

[69] N. Balakrishnan, R. C. Forrey, and A. Dalgarno, Phys. Rev. Lett. **80**, 3224 (1998).

[70] N. Balakrishnan *et al.*, Astrophys. J. **524**, 1122 (1999).

[71] R. C. Forrey, V. Kharchenko, N. Balakrishnan, and A. Dalgarno, Phys. Rev. A **59**, 2146 (1999).

[72] N. Balakrishnan, A. Dalgarno, and R. C. Forrey, J. Chem. Phys. **113**, 621 (2000).

[73] N. Balakrishnan and A. Dalgarno, J. Phys. Chem. A **105**, 2348 (2001).

[74] E. Bodo, F. A. Gianturco, and A. Dalgarno, Chem. Phys. Lett. **353**, 127 (2002).

[75] J. C. Flasher and R. C. Forrey, Phys. Rev. A **65**, 032710 (2002).

[76] T. Stoecklin, A. Voronin, and J. C. Rayez, Phys. Rev. A **66**, 042703 (2002).

[77] E. Hudson *et al.*, in preparation, (2005).

[78] P. F. Weck and N. Balakrishnan, J. Chem. Phys. **122**, 154309 (2005)

[79] N. Balakrishnan and A. Dalgarno, Chem. Phys. Lett. **341**, 652 (2001).

[80] N. Balakrishnan and A. Dalgarno, J. Phys. Chem. A **107**, 7101 (2003).

[81] J. L. Bohn, Phys. Rev. A **62**, 032701 (2000).

[82] R. V. Krems *et al.*, Phys. Rev. A **67**, 060703 (R) (2003).

[83] H. Cybulski *et al.*, J. Chem. Phys. **122**, 094307 (2005).

[84] K. Maussang *et al.*, Phys. Rev. Lett. **94**, 123002 (2005).

[85] A. Volpi and J. L. Bohn, Phys. Rev. A **65**, 052712 (2002).

[86] J. L. Bohn, Phys. Rev. A **63**, 052714 (2001).

[87] A. V. Avdeenkov and J. L. Bohn, Phys. Rev. A **66**, 052718 (2002).

[88] A. V. Avdeenkov and J. L. Bohn, Phys. Rev. A **71**, 022706 (2005).

[89] R. V. Krems and A. Dalgarno, J. Chem. Phys. **120**, 2296 (2004).

[90] A. V. Avdeenkov and J. L. Bohn, Phys. Rev. Lett. **90**, 043006 (2003).

[91] A. V. Avdeenkov and J. L. Bohn, Phys. Rev. A **69**, 012710 (2004).

[92] C. Ticknor and J. L. Bohn, Phys. Rev. A **71**, 022709 (2005).

[93] C. Ticknor and J. L. Bohn, submitted to Phys. Rev. A (2005).

[94] R. V. Krems, Int. Rev. Phys. Chem., in press. (2005).

[95] R. V. Krems, Phys. Rev. Lett. **93**, 013201 (2004).

[96] J. D. Jackson, *Classical Electrodynamics* (2nd Edition, Wiley, New York, 1975).

[97] J. Brown and A. Carrington, *Rotational Spectroscopy of Diatomic Molecules*, (Cambridge, Cambridge, 2003).

[98] D. M. Brink and G. R. Satchler, *Angular Momentum*, (Clardeon Press, Oxford, 1993).

[99] M. Tinkham, *Group Theory and Quantum Mechanics*, (Dover, New York, 2003).

[100] K. Schreel and J. J. ter Muelen, J. Phys. Chem. A **101**, (1997).

[101] T. Hain, R. Moision, and T. Curtiss, J. Chem. Phys. **111**, 6797 (1999).

[102] C. H. Townes and A. L. Schawlow *Microwave Spectroscopy*, (Dover, New York, 1975).

[103] G. Herzberg *Molecular Spectra and Molecular Structure: vol. 1 Spectra of Diatomic molecules*. (Kreiger, Florida, 1950).

[104] J. Taylor, *Scattering Theory*, (Krieger, Florida, 1983).

[105] M. S. Child, *Molecular Collision Theory*, (Dover, New York, 1974).

[106] James Burke, Ph.D Thesis. University of Colorado (1999).

[107] H. R. Sadeghpour *et al.*, J. Phys. B: At. Mol. Opt. Phys. **33** R93 (2000).

[108] B. R. Johnson, J. Comput. Phys. **13**, 445 (1973).

[109] S. Y. T. Meerakker *et. al*, physics/0407116 (2004).

[110] J. L. Bohn, Phys. Rev. A **62**, 032701 (2000).

[111] R. V. Krems, A. Dalgarno, N. Balakrishnan, and G. C. Groenenboom, Phys. Rev. A, **67** 060703(R) (2003).

[112] R. V. Krems and A. Dalgarno, J. Chem. Phys., **120** 2296 (2004); R. V. Krems, H.R. Sadeghpour, A. Dalgarno, D. Zgid, J. Klos, and G. Chalasinski, Phys Rev. A, **68** 051401(R) (2004).

[113] N. R. Claussen *et al.*, Phys. Rev. A **67**, 060701 (2003); E. G. M. van Kempen *et al.*, Phys. Rev. Lett. **88**, 093201 (2002); K. M. O'Hara *et al.* Phys. Rev. A **66**, 041401(R) (2002); C. Chin *et al.* Phys. Rev. Lett. **85**, 2717 (2000); J. P. Leo *et al.*, Phys. Rev. Lett. **85**, 2721 (2000).

[114] J. L. Bohn, A. V. Avdeenkov, and M. P. Deskevich, Phys. Rev. Lett. **89**, 203202 (2002).

[115] N. Balakrishnan, R. C. Forrey, and A. Dalgarno, Phys. Rev. Lett. **80**, 3224 (1998).

[116] R. V. Krems, Phys Rev. Lett. **93**, 13201 (2004).

[117] M. Marinescu and L. You, Phys Rev. Lett. **81**, 4596 (1998); S. Yi and L. You, Phys. Rev. A **63**, 053607 (2001).

[118] B. Deb and L. You, Phys. Rev. A **64**, 022717 (2001).

[119] A. Derevianko, S. G. Porsev, S. Kotochigova, E. Tiesinga, and P. S. Julienne, Phys. Rev. Lett. **90**, 063002 (2003).

[120] R. Santra *et al.*, Phys. Rev. A **67**, 062713 (2003).

[121] G. D. Stevens *et al.*, Phys Rev. A **53**, 1349 (1996).

[122] J. F. Baugh *et al.*, Phys Rev. A **58**, 1585 (1998).

[123] M. J. Seaton, Rep. Prog. Phys. **46** 167 (1983).

[124] M. Aymar *et al.*, Rev. Mod. Phys. **68**, 1015 (1996).

[125] C. Haimberger *et al.*, Phys. Rev. A **70**, 021402 (R) (2004); A. J. Kerman *et al.*, Phys. Rev. Lett. **92**, 153001 (2004); D. Wang *et al.*, Phys. Rev. Lett. **93**, 243005 (2004); M. W. Mancini *et al.*, Phys. Rev. Lett. **92**, 133203 (2004).

[126] D. DeMille, D. R. Glenn, and J. Petricka, Eur. Phys. J. D **31**, 375-384 (2004).

[127] U. Fano and A. R. P. Rau, *Atomic Collisions and Spectra* (Academic Press, London, 1986).

[128] C. H. Greene and Ch. Jungen, Adv. At. Mol. Phys. **21**, 51 (1985).

[129] F. H. Mies, J. Chem. Phys. **80**, 2514 (1984).

[130] B. Gao, Phys. Rev. A **58**, 4222 (1998); *ibid.* **62**, 050702 (2000).

[131] J. P. Burke, Jr., C. H. Greene, and J. L. Bohn, Phys. Rev. Lett. **81**, 3355 (1998).

[132] F. H. Meis and M. Raoult, Phys. Rev. A **62**, 012708 (2000).